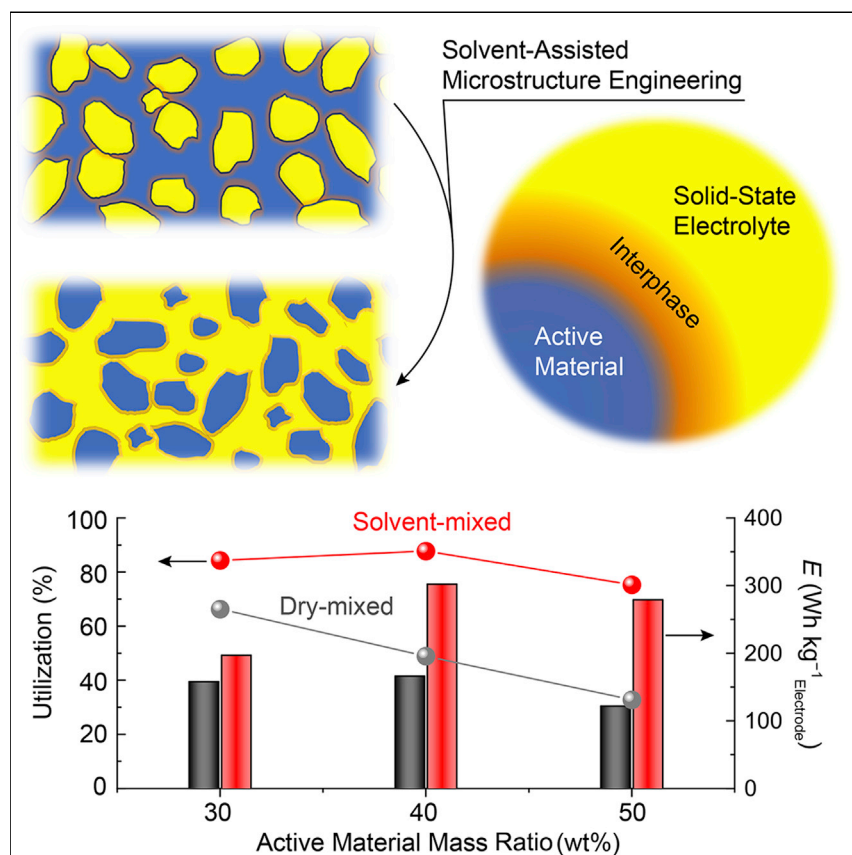


Article

Microstructure engineering of solid-state composite cathode via solvent-assisted processing



This work describes a successful integration of high-energy organic cathode materials into all-solid-state batteries, opening up an alternative pathway toward high-energy solid-state-lithium batteries, currently dominated by high-nickel layered oxide cathodes. An 80% increase in electrode-level specific energy is demonstrated by exploring a solvent-assisted process and better understanding the processing-microstructure-performance relationship. Characterization tools reveal critical chemical information of interfacial reaction products.

Jibo Zhang, Zhaoyang Chen, Qing Ai, ..., Hua Guo, Jun Lou, Yan Yao

yyao4@uh.edu

Highlights

Unoptimized electrode microstructure is the origin of low utilization of active materials

A solvent-assisted process could rectify the microstructure to improve utilization

Unique interphase redox chemistry between organic material and electrolyte is revealed

Article

Microstructure engineering of solid-state composite cathode via solvent-assisted processing

Jibo Zhang,¹ Zhaoyang Chen,¹ Qing Ai,² Tanguy Terlier,³ Fang Hao,¹ Yanliang Liang,¹ Hua Guo,² Jun Lou,² and Yan Yao^{1,4,*}

SUMMARY

Microstructure engineering of composite cathodes in all-solid-state batteries is critical to ensure efficient electronic and ionic percolation networks. Organic-based solid-state batteries have recently emerged with impressive material-level specific energy and cycling stability. However, the low mass fraction of active materials in state-of-the-art organic cathodes severely limits electrode-level specific energy. In this work, we reveal the unfavorable microstructure as the origin of poor performance at a high fraction of active materials; a solvent-assisted process is then devoted to rectifying the microstructure, increasing the active materials fraction from 20 to 40 wt % while maintaining high utilization (97.6%). The resulting electrode-level specific energy of 302 Wh kg⁻¹ is 83% higher than state-of-the-art solid-state batteries with organic cathodes. On the basis of the unique interphase chemistry between pyrene-4,5,9,10-tetraone and lithium thiophosphate, a potential-dependent reversible interphase evolution model is proposed. This work illustrates the critical role of microstructure engineering in optimizing novel active materials for all-solid-state batteries.

INTRODUCTION

Research on all-solid-state lithium metal batteries (ASSLBs) has flourished thanks to the potential benefits of higher energy density, improved safety, and wider operating temperature window made possible by high-conductivity solid-state electrolytes (SEs).^{1–3} Among various types of SEs,^{4–6} sulfide-based SEs exhibit considerably high ionic conductivity (>1 mS cm⁻¹ at 25°C), and have been widely utilized in ASSLBs due to the facile synthesis and processing procedures.^{7–10} During the operation of ASSLBs, Li-ion and electronic conductive agents are required to form percolating networks that sustain the electrochemical reactions of cathode active materials (CAM).^{11–13} Therefore, engineering the cathode microstructure is essential for efficient charge transport in maximizing the utilization of CAMs (Figure 1). Recent studies have demonstrated theoretical and experimental approaches in optimizing microstructures of lithium transition metal oxides (LMOs)-based cathodes in ASSLBs.^{14–16} Approaches such as controlling LMOs particle size¹⁷ and cathode-to-SE particle size ratio¹⁸ lead to improved utilization at a high active mass fraction (f_{CAM}). Furthermore, a comprehensive model has been developed to evaluate the effects of cathode composition, porosity, and particle size on the microstructure.¹⁹ Based on such knowledge, f_{CAM} as high as 85 wt % has been realized for LMOs.²⁰

The limited resources of Co or Ni used in producing LiCoO₂ and LiNi_xMn_yCo_{1-x-y}O₂ (NMC) calls for alternative cathode chemistries with advantages in material

Context & scale

Operation of solid-state electrodes requires a favorable percolation of Li⁺ ions and electrons to sustain the redox reaction of active materials; hence, the microstructure of a composite electrode should be optimized. Although the microstructure of oxide-based electrodes has been studied, the knowledge of soft and ductile active material, such as organic redox-active compounds, is still lacking. In this work, we present a study on the microstructure of organic-based electrodes. A solvent-mixing process is developed to regulate the cathode microstructure by exploiting the unique chemistry between cathode active materials and solid electrolytes. We report an organic-based cathode with comparable specific energy to inorganic cathodes. This work opens the door to using organic materials with controllable molecular design and a sustainable source for practical solid-state batteries.

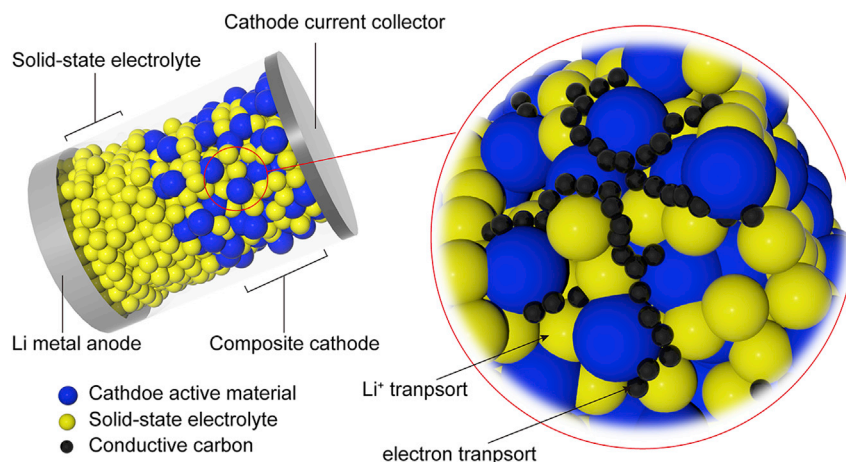


Figure 1. Schematic of an ASSLB and percolating networks for Li-ion and electron in composite cathode

Particle size is not proportional to the scale.

abundance. Organic battery electrode materials (OBEMs) are organic compounds with well-understood redox-active functional groups that enable reversibly storage/release of multiple electrons and cations per molecule.^{21,22} OBEMs with properties such as moderate redox potential, mechanical softness, and relatively small volume change during cycling have enabled some of the most stable solid-state batteries based on ceramic electrolytes.²³

Despite the favorable properties, demonstration of high-energy solid-state batteries with OBEMs is yet to be achieved. Previously, we demonstrated the first ceramic electrolyte-based organic batteries using sodium rhodizonate, which has a comparatively moderate theoretical capacity of 205 mAh g⁻¹.²⁴ Luo et al. later used a carboxylated azo compound with a slightly higher theoretical capacity of 231 mAh g⁻¹ but showed poor material utilization of 55%.²⁵ In 2019, we explored pyrene-4,5,9,10-tetraone (PTO), a quinone with a high theoretical capacity of 409 mAh g⁻¹, in solid-state batteries and demonstrated its active material utilization of 79% at 0.1 C rate.²³ Recently, we further improved the utilization to 99.5% by adopting a cryo-milling process.²⁶

While OBEMs with higher theoretical capacity has been utilized in ASSLBs and close to unity utilization have been demonstrated, one remaining challenge is the low f_{CAM} (20 wt % in Hao et al.²⁶) Attempts to increase f_{PTO} to 40 and 60 wt % result in decreased PTO utilization. In other words, the electrode-level specific energy ($E_{Electrode}$)—defined as the energy normalized by total electrode mass—of state-of-the-art organic-based solid-state batteries remains low (up to 165 Wh kg⁻¹, [Table S1](#)). In contrast to inorganic-based ASSLBs,^{16–18} very little work has been done on microstructure optimization for organic-based solid-state batteries.

In this work, we report a solvent-mixing process that leads to a high PTO utilization (97.6%) at an f_{PTO} of 40 wt % and an electrode-level specific energy of 302 Wh kg⁻¹ ([Table S1](#)), an 83% improvement on state-of-the-art solid-state batteries with OBEMs. In a conventional dry-mixed electrode, the origin of reduced PTO utilization was found to be related to the unfavorable microstructure. A solvent-mixing process, which preforms “core-shell” PTO-SE particles, has been demonstrated to be

¹Department of Electrical and Computer Engineering and Texas Center for Superconductivity at the University of Houston (TcSUH), University of Houston, Houston, TX 77204, USA

²Department of Materials Science and NanoEngineering, Rice University, Houston, TX 77005, USA

³SIMS laboratory, Shared Equipment Authority, Rice University, Houston, TX 77005, USA

⁴Lead contact

*Correspondence: yyao4@uh.edu

<https://doi.org/10.1016/j.joule.2021.05.017>

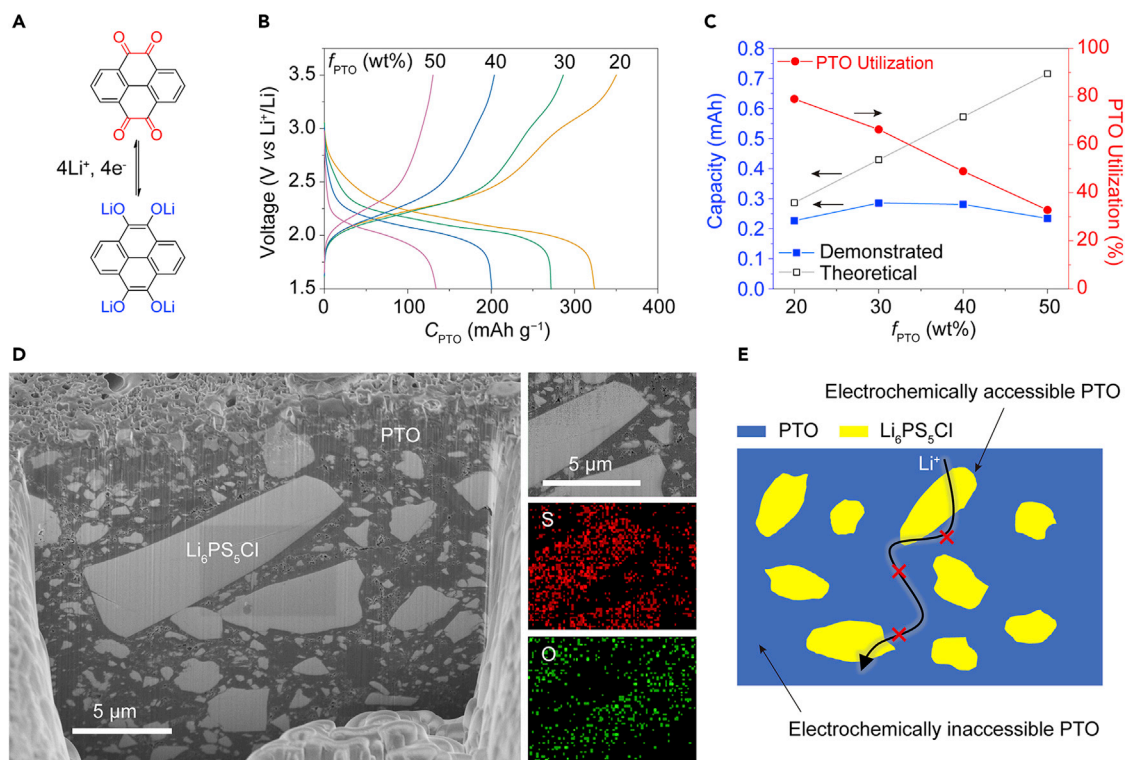


Figure 2. Low PTO utilization of dry-mixed cathodes and its origin in the unfavorable microstructure of cathode composite

(A) Molecular structure of PTO and electrochemical reaction for Li-ion storage.

(B) Galvanostatic voltage profiles for dry-mixed cathodes at 0.1C, 60°C. 1C = 409 mA g⁻¹.

(C) Demonstrated capacity and utilization change as f_{PTO} increases.

(D) FIB-SEM and EDS cross-section images a dry-mixed cathode ($f_{\text{PTO}} = 40$ wt %).

(E) Schematic illustration of an unfavorable microstructure with a disconnected Li⁺ percolating network that results in an electrochemically inaccessible PTO.

effective in rectifying the microstructure and improving the electrochemical performance. A suite of characterization techniques including focused ion beam-scanning electron microscopy (FIB-SEM), time-of-flight secondary ion mass spectrometry (ToF-SIMS), X-ray photoelectron spectroscopy (XPS), and electrochemical impedance spectroscopy (EIS) was employed to quantify the chemical composition and spatial distribution of the interphase as the result of a spontaneous redox reaction between PTO and Li₆PS₅Cl.

RESULTS AND DISCUSSION

Origin of low PTO utilization in dry-mixed cathodes

ASSLBs with a cell configuration of Li | Li₃PS₄ | PTO:Li₆PS₅Cl:C were assembled. PTO has a theoretical specific capacity of 409 mAh g⁻¹ from the redox reaction of four carbonyl groups (Figure 2A). Argyrodite Li₆PS₅Cl was used in the cathode due to its high Li⁺ conductivity and solution processability.²⁷ Li₃PS₄ was employed as the electrolyte layer due to its interfacial stability with Li metal anode.²⁸ The composite cathodes were prepared by a dry-mixing process, where PTO, Li₆PS₅Cl and conductive carbon (super C65) were mixed by pestle and mortar at a mass ratio of x:(90-x):10 for PTO: Li₆PS₅Cl: C65, where x represents the mass fraction of PTO, followed by uniaxial compaction. Cells with a constant mass (3.5 mg) but different active material ratios ($f_{\text{PTO}} = 20, 30, 40, 50$ wt %) were fabricated and characterized. As shown in

Table 1. Electrochemical performance of dry- and solvent-mixed cathodes

Dry-mixed, f_{PTO} (wt %)	m_{PTO} (mg)	Theoretical capacity (mAh)	Demonstrated capacity (mAh)	Utilization (%)	C_{PTO} (mAh g ⁻¹)
20	0.70	0.286	0.227	79.0	323
30	1.05	0.430	0.285	66.3	271
40	1.40	0.573	0.281	48.9	200
50	1.75	0.716	0.234	32.8	134
Solvent-mixed, f_{PTO} (wt %)	m_{PTO} (mg)	Theoretical capacity (mAh)	Demonstrated capacity (mAh)	Utilization (%)	C_{PTO} (mAh g ⁻¹)
30	1.05	0.430	0.363	84.4	345
40	1.40	0.573	0.503	87.8	359
40 (BM-PTO)	1.40	0.573	0.558	97.6	399
50	1.75	0.716	0.541	75.3	308

The total mass of cathode was kept constant at 3.5 mg.

Figures 2B and 2C, a cell with an f_{PTO} of 20 wt % exhibits a specific capacity (C_{PTO}) of 323 mAh g⁻¹ at 0.1C, corresponding to 79.0% PTO utilization. When f_{PTO} increases to 50 wt %, C_{PTO} and utilization decrease to 134 mAh g⁻¹ and 32.8%, respectively. Table 1 summarizes the key performance parameters of dry-mixed cathodes.

To identify the origin of low PTO utilization, we studied the contribution from each component of a cell. The anode was first studied as illustrated in Figure S1. First, a Li/Li₃PS₄/Li cell was fabricated and cycled at the current density equivalent to that of a full cell, e.g., 55 $\mu\text{A cm}^{-2}$ when f_{PTO} is 50 wt %. The overpotential for Li plating/stripping is as small as 4 mV and remains stable, suggesting the Li/Li₃PS₄ interface is not the culprit. Second, the microstructure of composite cathode was investigated. By exposing the cross-section via FIB-SEM, we observed an “electrolyte-in-active material”-type microstructure (Figure 2D)—Li₆PS₅Cl with a size between 2 to 15 μm was surrounded by PTO—which was confirmed by energy dispersive spectroscopy (EDS) mapping. The distribution of Li₆PS₅Cl and PTO is unfavorable for Li⁺ transport since Li₆PS₅Cl is isolated by Li⁺-insulating PTO phase (Figure 2E). The contact area between Li₆PS₅Cl and PTO is relatively small, limiting the volume of electrochemically accessible PTO. Third, *operando* EIS was conducted to examine the interphase of PTO-Li₆PS₅Cl. The impedance evolutions during the first two cycles for both samples (f_{PTO} = 20 and 40 wt %) show excellent reversibility (Figures S2 and S3), in agreement with the previous observation from the Li₃PS₄-PTO system.²⁶ The above analysis points to the unfavorable microstructure as the most likely cause of low PTO utilization at high f_{PTO} .

Reverse nonideal microstructure by a solvent-assisted process

The fabrication process can greatly impact the microstructure of a cathode. During dry mixing where the uniaxial pressure applies on loosely packed particles (Figure 3A), PTO may experience greater deformation than Li₆PS₅Cl owing to its lower elastic modulus and higher ductility, thus resulting in the undesired microstructure. The study on the mechanical properties of cathode composite by nanoindentation will be reported in the future.

Here, we present an effective strategy to overcome this issue by solvent-mixing. The objective is to preform “core-shell” particles for cathode compaction, where a PTO core is surrounded by a Li₆PS₅Cl shell. We hypothesize the deformation of PTO during uniaxial pressing could be confined by preforming the “core-shell” particles, therefore breaking the continuous PTO domain and reversing the “electrolyte-in-active material”-type microstructure (Figure 3A). To achieve this goal, the solvent for the solvent-mixing process should dissolve Li₆PS₅Cl whereas barely dissolve

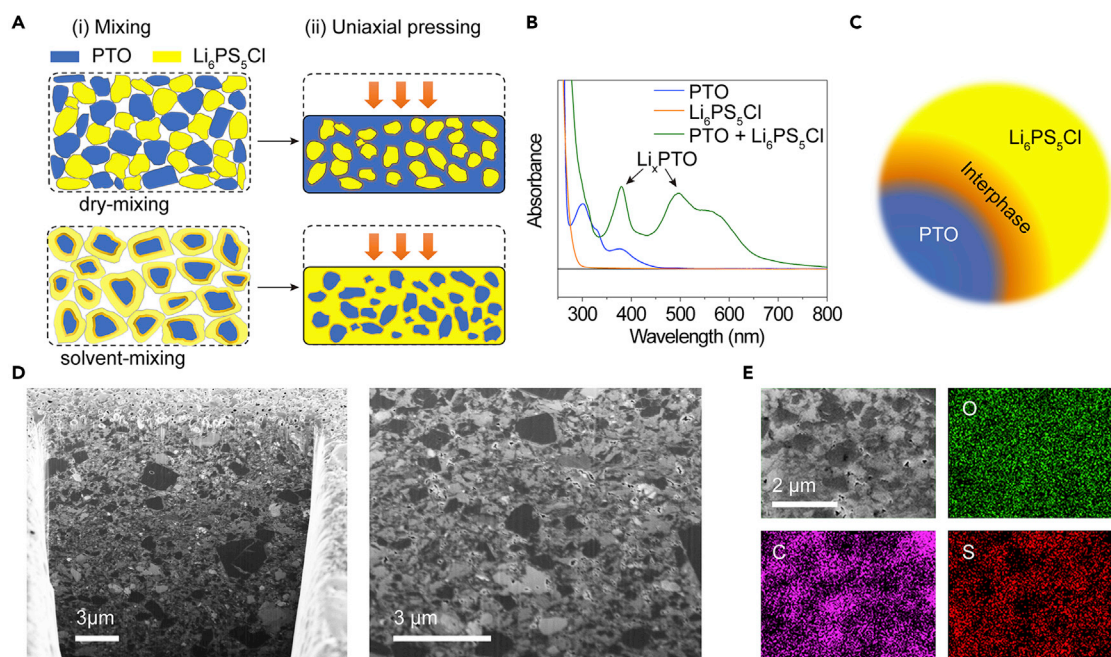


Figure 3. Solvent-mixing regulates the cathode microstructure via an *in situ* formed interphase

(A) The two-step preparation for dry- and solvent-mixed cathodes. (i) Mixing PTO and $\text{Li}_6\text{PS}_5\text{Cl}$ powders in a dry or solvent-assisted fashion. (ii) Powder compaction by uniaxial pressing.

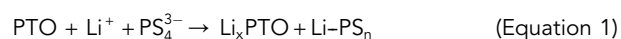
(B) UV-vis spectra on the spontaneous redox reaction between PTO and $\text{Li}_6\text{PS}_5\text{Cl}$. The spectra were recorded in a CH_3CN -ethanol mixed solvent.

(C) Schematic of a PTO-interphase- $\text{Li}_6\text{PS}_5\text{Cl}$ "core-shell" structure resulting from solvent-assisted mixing.

(D and E) FIB-SEM (D) and EDS (E) cross-section images of a solvent-mixed cathode ($f_{\text{PTO}} = 40$ wt %), showing a uniform distribution of PTO and $\text{Li}_6\text{PS}_5\text{Cl}$.

PTO. For this reason, ethanol is selected. During solvent-mixing, PTO and conductive carbon were first mixed in ethanol to form a suspension. Once $\text{Li}_6\text{PS}_5\text{Cl}$ was added, the mixture immediately turned black. The color change can be explained by the reaction of the surface of PTO particles with the dissolved $\text{Li}_6\text{PS}_5\text{Cl}$. Owing to the moderate oxidizing strength of PTO (2.9 V versus Li^+/Li , Figure S4), a spontaneous redox reaction between PTO and the PS_4^{3-} tetrahedron in $\text{Li}_6\text{PS}_5\text{Cl}$ occurs, leading to partially reduced PTO (Li_xPTO), as evidenced by the new peaks emerged in UV-vis spectra (Figure 3B, a detailed discussion on the UV-vis spectra analysis is summarized in Note S1). Simultaneously, $\text{Li}_6\text{PS}_5\text{Cl}$ is partially oxidized to form lithium poly-thiophosphates (Li-PS_n) which contain bridging sulfur ($-\text{[S]}_n-$) moieties.^{29–31} Although ethanol leads to slight decomposition of $\text{Li}_6\text{PS}_5\text{Cl}$ after annealing, ethanol remains as the only effective candidate for solvent-mixing so far. Further optimization of processing solvents should be focused on candidates with a proper solubility while minimizing the structural change of $\text{Li}_6\text{PS}_5\text{Cl}$.³² We propose a mixed solvent strategy that combinations of solvents of different polarity will be explored in the future.

Equation 1 is a skeleton equation (stoichiometrically unbalanced due to the complicated oxidation products of lithium thiophosphate) which describes the redox reaction between PTO and $\text{Li}_6\text{PS}_5\text{Cl}$.



Similar redox reaction may take place in the dry-mixed cathode, where the peaks of $-\text{[S]}_n-$ appear at 163.6 and 164.8 eV in the XPS spectra (Figure S5). The solvent-mixed cathode contains higher CAM/solid electrolyte interfacial area.

After solvent evaporation and thermal annealing, a PTO-interphase- $\text{Li}_6\text{PS}_5\text{Cl}$ “core-shell” structure will form (Figure 3C). The thermal stability of PTO limits the annealing temperature of the solvent-mixed cathode, based on which an ionic conductivity of 6.2×10^{-5} S/cm (at 60°C) is recovered for $\text{Li}_6\text{PS}_5\text{Cl}$. Although this value enables a proof-of-concept demonstration in the present study, a thorough optimization of the annealing conditions is necessary to further enhance the cathode performance. The chemical composition of the interphase will be discussed in the next section. The core-shell powders enable the change of microstructure when the powders are subjected to compaction. The cross-section of a solvent-mixed cathode ($f_{\text{PTO}} = 40$ wt %) prepared by FIB-SEM was imaged with EDS mapping. Figures 3D and 3E show an “active material-in-electrolyte”-type microstructure where the $\text{Li}_6\text{PS}_5\text{Cl}$ domain (gray) now forms a continuous network with an embedded PTO domain (black). Furthermore, greatly reduced SE domain size suggests much enhanced interphase area. A similar fine distribution of the PTO and $\text{Li}_6\text{PS}_5\text{Cl}$ domains can also be achieved in the solvent-mixed cathode with f_{PTO} of 50 wt % (Figure S6).

ToF-SIMS analysis of composite cathodes

ToF-SIMS correlates the chemical information with spatial distributions of cathode components. During the measurements, secondary ions (SIs) are generated by the fragmentation of sample species under the collision cascade of energetic incident ions (Bi_3^+) (Figure 4A). A cesium sputter ion beam (Cs^+) is further applied for axial resolution. Hence, the compositions of the SIs are strongly related to the local chemical environment in the cathode. A combined analysis of the SI mapping and mass spectra enables the identification of fingerprinting fragments from PTO, $\text{Li}_6\text{PS}_5\text{Cl}$, and the interphase, respectively (Table S2; Figures S7–S10). For example, Li- and C-rich fragments ($\text{Cs}_2\text{LiC}_2^+$ and $\text{Cs}_2\text{LiC}_4^+$ at the m/z of 296.8 and 320.8, respectively) originate from the fragmentation of Li_xPTO . Therefore, mapping of $\text{Cs}_2\text{LiC}_2^+$ reveals the spatial distribution of the interphase.

Figures 4B and 4C visualize the distributions of fragments corresponding to the interphase ($\text{Cs}_2\text{LiC}_2^+$, green), $\text{Li}_6\text{PS}_5\text{Cl}$ ($^6\text{Li}^+$, blue), and PTO (Cs_3C_2^+ , red) in pristine cathodes. More intense formation of the interphase in the solvent-mixed cathode is found with higher intensity of interphase fragments (Figure S10). Complementary distribution of PTO and $\text{Li}_6\text{PS}_5\text{Cl}$ phases corroborates the morphology observed from FIB-SEM. In dry-mixed cathodes, the $\text{Li}_6\text{PS}_5\text{Cl}$ domains are greater than $10 \mu\text{m}$ in diameter and separated by the PTO phase, whereas in solvent-mixed cathodes, the $\text{Li}_6\text{PS}_5\text{Cl}$ domains are greatly reduced in size and a uniform mixing with PTO is achieved.

Reconstructed 3D structures illustrate the percolating network within cathodes (Figures 4D and S11). $\text{Li}_6\text{PS}_5\text{Cl}$ domains are poorly connected in the dry-mixed cathode, limiting the utilization of PTO by impeding Li^+ transport. On the contrary, solvent-mixed cathode exhibits a well-connected $\text{Li}_6\text{PS}_5\text{Cl}$ network that surrounds PTO, which will greatly enhance the electrochemically accessible volume fraction of PTO through sufficient and intimate contact with $\text{Li}_6\text{PS}_5\text{Cl}$, thus an increased utilization of PTO.

Electrochemical reversibility of the interphase

To probe the electrochemical activity and evolution of the interphase in a solvent-mixed cathode, we performed *operando* EIS measurements during initial cycles. Figure 5A shows the galvanostatic voltage profiles and the Warburg coefficients (A_w) extracted from the low-frequency region (1.0–0.1 Hz) in the Nyquist plots (Figure 5B). During the first cycle, A_w decreased from $62 \Omega \text{ s}^{-1/2}$ at open circuit voltage

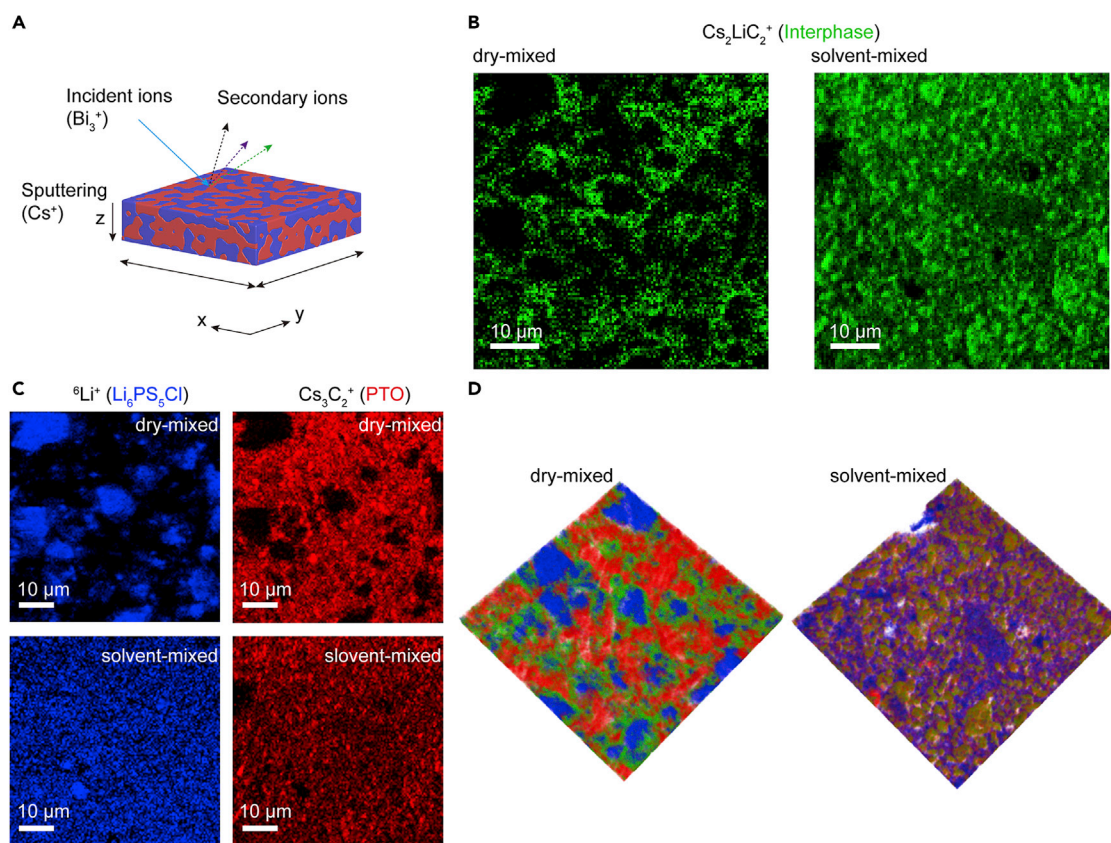


Figure 4. ToF-SIMS imaging of PTO, $\text{Li}_6\text{PS}_5\text{Cl}$, and interphase in pristine dry- and solvent-mixed cathodes

(A) Schematic of ToF-SIMS analysis with an area of $60 \times 60 \mu\text{m}^2$.

(B and C) 2D SI images showing the distribution of interphase ($\text{Cs}_2\text{LiC}_2^+$), $\text{Li}_6\text{PS}_5\text{Cl}$ (${}^6\text{Li}^+$), and PTO (Cs_3C_2^+), as represented by respective characteristic fragments listed in parentheses.

(D) Reconstructed 3D microstructure of dry- and solvent-mixed cathodes, showing the distribution of PTO (red), $\text{Li}_6\text{PS}_5\text{Cl}$ (blue) and interphase (green).

to $46 \Omega \text{ s}^{-1/2}$ at 1.5 V versus Li^+/Li (Figure S12; Table S3) and then remained less than $100 \Omega \text{ s}^{-1/2}$ during charging. Once the voltage reached 2.5 V versus Li^+/Li , the oxidation onset potential of $\text{Li}_6\text{PS}_5\text{Cl}$, a significant increase of A_W to $1,310 \Omega \text{ s}^{-1/2}$ was observed. Interestingly, A_W reverted to $55 \Omega \text{ s}^{-1/2}$ at 2.0 V during the second discharge and remained low until the next charging. A similar pattern of A_W evolution was observed during the second and third cycles. Such periodical variation of A_W shows the electrochemical reversibility of the interphase and indicates a dynamic evolution mechanism.

To provide chemical information for the reversibility of the interphase, we conducted *ex situ* XPS on pristine and cycled solvent-mixed cathodes (see also Figures S13 and S14). As shown in Figure 5C, the XPS spectrum of sulfur species of the pristine cathode exhibits two major doublets with S $2p_{3/2}$ peaks at 161.7 and 163.6 eV, respectively. The former originates from the lithium-thiophosphate unit ($-\text{S}-\text{Li}$) and the latter is ascribed to $-\text{[S]}_n^-$ from $\text{Li}-\text{PS}_n$.^{31,33,34} The component at 163.6 eV greatly decreased and the peak at 161.7 eV became predominant in a discharged cathode, suggesting the reduction of $-\text{[S]}_n^-$ to $-\text{S}-\text{Li}$. After subsequent charging to 3.5 V (versus Li^+/Li), the peak intensity at 163.6 eV regained. Based on the EIS and XPS data, a potential-dependent interphase evolution model is proposed (Figure 5D). The interphase consists of Li_xPTO and $\text{Li}-\text{PS}_n$ in a pristine solvent-mixed cathode. As discharging

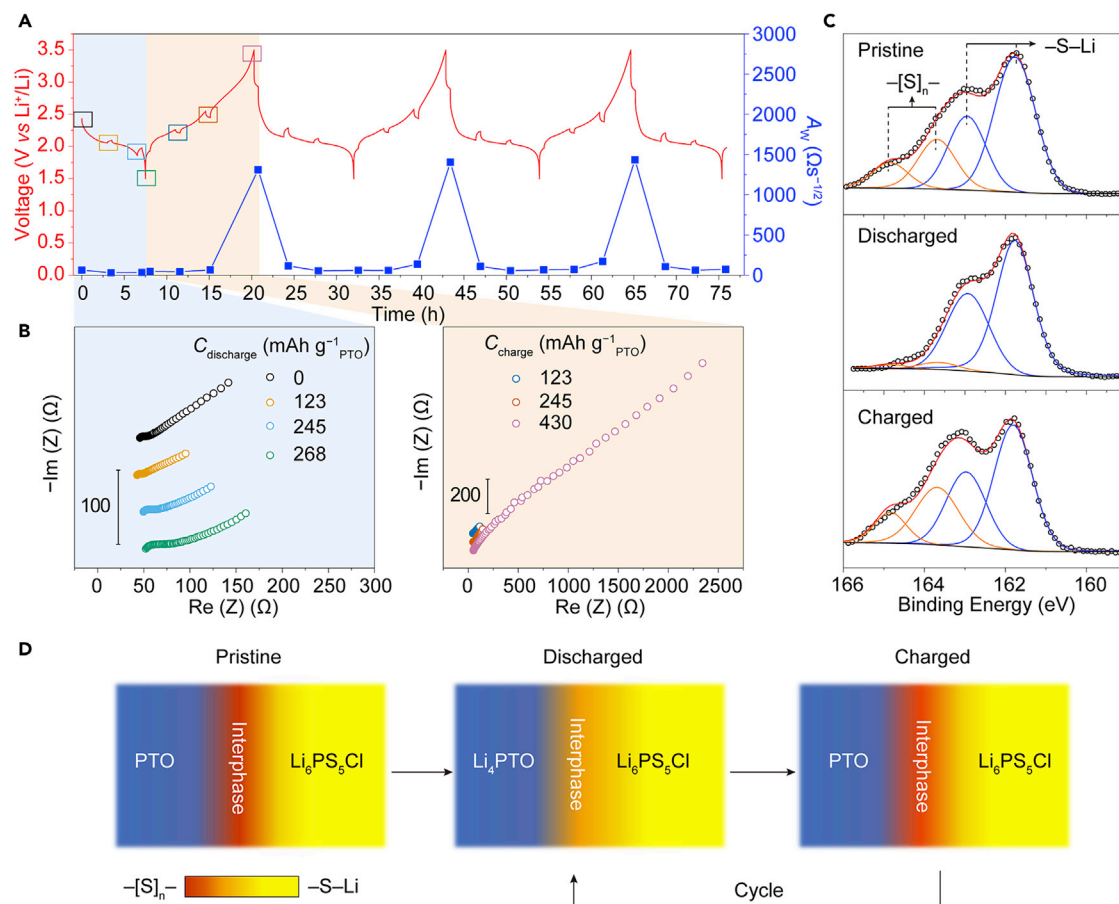


Figure 5. Electrochemical reversibility of interphase in solvent-mixed cathodes

(A and B) Intermittent galvanostatic voltage profile recorded at 0.1C and corresponding A_W (A) calculated from the corresponding Nyquist plots (B). (C) XPS spectra of a solvent-mixed cathode at pristine, discharged, and charged states in the S 2p region. (D) Schematics of the potential-dependent evolution model of interphase.

proceeds, PTO is reduced to Li_4PTO and $-\text{[S]}_n^-$ is reduced to $-\text{S-Li}$. In the subsequent charging, Li_4PTO becomes delithiated and $-\text{S-Li}$ remains stable under low anodic potentials (~ 2.5 V versus Li^+/Li). Further increasing the voltage results in full charging of PTO and oxidation of $-\text{S-Li}$ to $-\text{[S]}_n^-$. The distribution of $-\text{S-Li}$ and $-\text{[S]}_n^-$ at different potentials is further plotted in Figure S15. Since Li-PS_n has a lower Li^+ conductivity than $\text{Li}_6\text{PS}_5\text{Cl}$, its accumulation decreases the local Li^+ diffusivity and leads to an increased A_W . Fitting of EIS data reveals that the charge-transfer kinetics remains favorable within the working voltage and is slightly hindered at the end of charge (Table S4). Finally, the moderate voltage of PTO (1.5–3.5 versus Li^+/Li) avoids the irreversible formation of species such as S and P_2S_5 ,^{29,30} and contributes to stable cycling of PTO that operates at voltages that slightly exceed the thermodynamic stability window of $\text{Li}_6\text{PS}_5\text{Cl}$. A detailed analysis of the multiple interfaces that may undergo electrochemical process within the cathode is summarized in Note S2.³⁵

Electrochemical performance of solvent-mixed cathodes

Solid-state cells with solvent-mixed cathodes with constant mass (3.5 mg) but various f_{PTO} were fabricated and characterized. When f_{PTO} increases from 30 to 50 wt %, cell capacity increases from 0.36 to 0.54 mAh (Figure 6A). Compared to

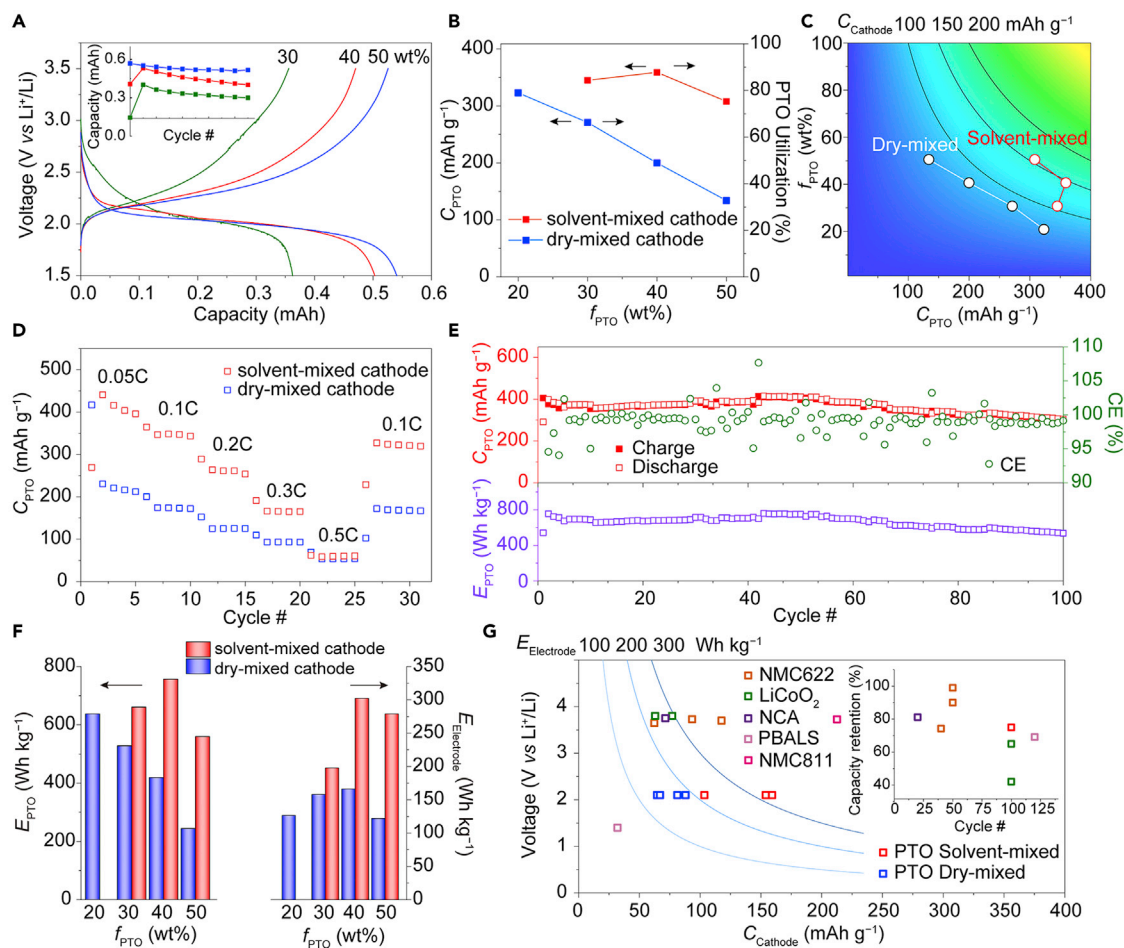


Figure 6. Electrochemical performance of solvent-mixed cathodes

All measurements were conducted at 60°C.

(A) Galvanostatic voltage profiles of solvent-mixed cathodes. Inset shows discharge capacity of the first 10 cycles at 0.1C ($f_{\text{PTO}} = 30, 40,$ and 50 wt %).

(B) Improved C_{PTO} and utilization of PTO.

(C) Enhanced C_{Cathode} of solvent-mixed cathodes at different f_{PTO} .

(D) Rate capabilities of cells with dry-mixed and solvent-mixed cathodes at $f_{\text{PTO}} = 40$ wt %.

(E) Cycling stability of the solvent-mixed cathode (BM-PTO) ($f_{\text{PTO}} = 40$ wt %) at 0.1C.

(F) Enhanced E_{PTO} and $E_{\text{Electrode}}$ of solvent-mixed cathodes.

(G) Comparison of $E_{\text{Electrode}}$ of PTO-based cathodes with state-of-the-art cathodes in ASSLBs. Inset shows capacity retention. Abbreviations: NMC622, $\text{LiNi}_{0.6}\text{Mn}_{0.2}\text{Co}_{0.2}\text{O}_2$; NMC811, $\text{LiNi}_{0.8}\text{Mn}_{0.1}\text{Co}_{0.1}\text{O}_2$; NCA, $\text{LiNi}_{0.80}\text{Co}_{0.15}\text{Al}_{0.05}\text{O}_2$; PBALS, 4-(phenylazo) benzoic acid lithium salt. See Table S1 for detailed information.

dry-mixed cathodes, solvent-mixed cathodes exhibit higher PTO utilization (Figure 6B; Table 1)—from 48.9% to 87.8% ($f_{\text{PTO}} = 40$ wt %) and from 32.8% to 75.3% ($f_{\text{PTO}} = 50$ wt %). When comparing capacity per electrode mass (C_{Cathode}), the solvent-mixed cathode reaches 154 mAh g^{-1} , almost twice that of the dry-mixed cathode (81 mAh g^{-1} , Figure 6C). To exclude the capacity contribution from the redox reaction of the electrolyte, a control cell consisting of $\text{Li}_6\text{PS}_5\text{Cl}$ and carbon (4:1 w/w) was fabricated. Generally, a high carbon content is required to facilitate the redox of SEs due to their low electronic conductivity.^{30,36,37} A detailed analysis of the cathode capacity is summarized in Note S3. Our data show that $\text{Li}_6\text{PS}_5\text{Cl}$ exhibits a specific capacity of only 15 mAh g^{-1} , less than 4% of the total capacity of solvent-mixed cathodes (Figures S16 and S17). Therefore, we conclude that the reported cathode capacities are predominantly contributed by PTO.

Solvent-mixed cathodes not only show higher capacity and utilization, but also exhibit faster kinetics (Figure 6D). At an f_{PTO} of 40 wt % and 0.3C, a solvent-mixed cathode shows a capacity of 166 mAh g⁻¹ compared with the 93 mAh g⁻¹ from a dry-mixed cathode. Such an improvement in electrochemical performance is rooted in the optimized microstructure.³⁸ To further reduce the particle size of PTO, PTO powders were first ball milled (BM-PTO) and then mixed with Li₆PS₅Cl during the solvent-mixing process ($f_{\text{PTO}} = 40$ wt %). The cell exhibits a high materials utilization of 97.6% with an initial C_{PTO} of 399 mAh g⁻¹ (Figure 6E). The cell shows a 75% capacity retention after 100 cycles with near-unity coulombic efficiency. Moreover, the cathode shows a high specific energy (E_{PTO}) of 755 Wh kg⁻¹, considering the mass of stoichiometric Li in the reaction.

$E_{\text{Electrode}}$, proposed earlier as an important figure-of-merit of ASSLBs, can be defined as the product of E_{CAM} and f_{CAM} . Figure 6F summarizes E_{PTO} and $E_{\text{Electrode}}$ for dry- and solvent-mixed cathodes used in this work and the literature with additional parameters presented in Table S1. Clearly, solvent-mixed cathodes exhibit the highest $E_{\text{Electrode}}$ value of 302 Wh kg⁻¹, not only outperforming dry-mixed cathodes but also greatly exceeding previously reported PBALS-based (45 Wh kg⁻¹)²⁵ and PTO-based (165 Wh kg⁻¹) ASSLBs. The $E_{\text{Electrode}}$ value demonstrated in this work is on par with that of NMC622,^{14,39,40} NMC811,²⁰ LiCoO₂,⁴¹ and NCA⁴²-based cells (Figure 6G). The PTO cells have advantages in cycling stability without using any coating layer on CAM. The average discharge voltage of a PTO cathode is lower than those of oxide-based cathodes (2.1 V for PTO versus 3.7 V for NMCs). From the application perspective, bipolar cell design could be an effective method to increase the output voltage. Notably, such a bipolar design could be relatively easily achieved in solid-state batteries.

In terms of electrode-level volumetric energy density, organic-based ASSLBs are lower than NMC-based ASSLBs due to the lower density of OBEMs (Table S5). Higher f_{CAM} or higher cathode loading can improve the energy density. Figure S18 shows a PTO-based ASSLBs with a 10-mg cathode loading, realizing an areal capacity of 1.1 mAh cm⁻². Further improvements in ionic conductivity by optimizing the fabrication conditions are expected to further improve areal capacity.

In conclusion, we show the impact of microstructure engineering on the performance of solid-state lithium batteries. We developed a solvent-mixing process to regulate the microstructure of electrodes containing ductile organic materials. The solvent-mixing of PTO and Li₆PS₅Cl forms the PTO-interphase-Li₆PS₅Cl "core-shell" structure which promotes the formation of a microstructure for efficient charge transport. With FIB-SEM, ToF-SIMS, EIS, and XPS, we studied the chemical composition, spatial distribution, and electrochemical reversibility of the interphase. As a result, the mass fraction of active materials has increased from 20 to 50 wt %. The new process enabled an electrode-level specific energy of 302 Wh kg⁻¹, an 83% improvement on state-of-the-art solid-state batteries with OBEMs. This value is on par with most inorganic cathodes. Further improvement is possible by fine-tuning the thermal annealing process and further increasing of f_{PTO} . We believe this work will benefit not only organic-based ASSLBs but also help microstructure optimization of solid-state lithium-sulfur batteries.

EXPERIMENTAL PROCEDURES

Resource availability

Lead contact

Further information and requests for resources should be directed to and will be fulfilled by the lead contact, Yan Yao (yyao4@uh.edu).

Materials availability

This study did not generate new reagents.

Data and code availability

The authors declare that the data supporting the findings of this study are available within the article and its [supplemental information](#) files.

Synthesis of PTO and Li_3PS_4

PTO was synthesized by the ruthenium-catalyzed oxidation of pyrene. Briefly, 10.1 g (50 mmol) pyrene (98%, Aldrich) was dissolved in 200 mL CH_2Cl_2 and 200 mL CH_3CN under stirring. Then 87.5 g (401 mmol) NaIO_4 (98%, Alfa Aesar), 1.25 g (6 mmol) $\text{RuCl}_3 \cdot x\text{H}_2\text{O}$ (98%, Oakwood Chemical) and 100 mL H_2O were added to the above solution. The mixture was stirred at 35°C for 15 h. The reaction mixture was washed by H_2O , and the dark green solid was collected by filtration. After the organic phase was separated, the filter liquor was extracted with 150 mL (3 × 50 mL) CH_2Cl_2 . The extracts were combined with the organic phase and the solvent was removed under reduced pressure. All the solid products were combined. Thin-layer chromatography (TLC) using CH_2Cl_2 /ethyl acetate (10/1) eluent revealed the presence of several by-products. Flash column chromatography using CH_2Cl_2 as eluent gave pure PTO as bright yellow crystals. PTO: yield 15%. ^1H NMR (500 MHz, $\text{DMSO}-d_6$) δ 8.33 (d, $J = 7.8$ Hz, 4H), 7.74 (t, $J = 7.8$ Hz, 2H). The solubility of PTO is too low for the ^{13}C NMR spectrum with acceptable accuracy.

Li_3PS_4 was synthesized by mechanochemical reaction followed by heat treatment. Briefly, 0.765 g Li_2S (99.9%, Sigma-Aldrich) and 1.235 g P_2S_5 (99%, Sigma-Aldrich) were ball milled in a 250 mL argon-protected stainless-steel jar with stainless-steel milling balls at 200 rpm for 2 h and at 500 rpm for 20 h. The powder was collected and annealed at 260°C under vacuum for 2.25 h to obtain glass-ceramic Li_3PS_4 .

Fabrication of solid-state lithium cells

$\text{Li}_6\text{PS}_5\text{Cl}$ (NEI) and super C65 conductive carbon black (MTI) were used as Li^+ and electron conducting agents in the composite cathodes, respectively. Composite cathodes were prepared by mixing PTO, $\text{Li}_6\text{PS}_5\text{Cl}$ and super C65 at a mass ratio of $x:(90-x):10$ for PTO: $\text{Li}_6\text{PS}_5\text{Cl}$: C65, where x represents the mass fraction of PTO (f_{PTO}). The dry process refers to a conventional mortar and pestle mixing method, during which PTO, $\text{Li}_6\text{PS}_5\text{Cl}$ and super C65 were added into the mortar and ground for 20 min. In the solvent-mixing process, PTO was first dispersed in ethanol with an agate mortar and pestle, followed by the addition of C65. Finally, $\text{Li}_6\text{PS}_5\text{Cl}$ was added into the mortar. Since $\text{Li}_6\text{PS}_5\text{Cl}$ is soluble in ethanol, the mixture was stirred to dry and further vacuum dried at 60°C. The powders were collected and annealed at 180°C for 0.5 h before being subjected to composite pressing. The solvent-mixed cathode for cycling stability test was prepared using BM-PTO at $f_{\text{PTO}} = 40$ wt %. BM-PTO was prepared by ball milling 200 mg of PTO powder in a 100 mL agate milling jar at 400 rpm for 10 h.

The SE-free cathode was prepared by mixing PTO with super C65 at a 1:1 weight ratio through a dry process. For the control cell without PTO in the cathode, 1.75 mg of the composite (1.40 mg pre-treated $\text{Li}_6\text{PS}_5\text{Cl}$ and 0.35 mg super C65) was used as cathode for the cell fabrication, reaching the same amount of $\text{Li}_6\text{PS}_5\text{Cl}$ and super C65 as in a composite cathode at $f_{\text{PTO}} = 50$ wt %. The pre-treated $\text{Li}_6\text{PS}_5\text{Cl}$ was prepared by dissolving pristine $\text{Li}_6\text{PS}_5\text{Cl}$ in ethanol, followed by drying and annealing at 180°C for 0.5 h. For solid-state Li symmetric cells, Li foils were attached to both sides of the Li_3PS_4 pellet.

Solid-state-lithium full cells were assembled with a polyetherether-ketone module (electrode area: 1.3 cm^2). Li_3PS_4 was used for the electrolyte layer due to its stability with Li metal. Briefly, 130 mg Li_3PS_4 powder was filled in a die and pressed under 150 MPa to form a pellet. Afterwards, the cathode powder was uniformly distributed on top of the Li_3PS_4 pellet, followed by pressing at 375 MPa. The pressed cathode has a porosity of 1% revealed from reconstructed 3D slice and view data by FIB-SEM. The mass of cathode was kept constant at 3.5 mg for all cells. The thickness of the cathode layer and SE pellet are 26 and 522 μm , respectively, as shown in Figure S6. A Li metal foil (thickness: 100 μm) on a stainless-steel current collector was attached to the other side of the Li_3PS_4 pellet as the anode.

Materials characterization

Cross sections of composite cathodes were imaged using a dual beam FIB-SEM (Helios NanoLab 660 DualBeam). The cross sections were obtained by Ga ion beam using 30 kV/47 nA for rough milling, and 30 kV/0.79 nA for fine polishing. The cycled cathodes were investigated by XPS (Physical Electronics PHI 5700). The XPS was produced via a monochromatic Al-K α X-ray source (1,486.6 eV) operated at 350 W (15 kV). The analyzed area is 0.8 μm diameter. The spectra were calibrated in relation to the signal of C 1s at 284.8 eV. We used the following fitting conditions for analyzing S 2p peaks: (1) Shirley background, (2) Gauss-Lorentz line-shape fitting on peaks, and (3) spin-orbit components ($\Delta = 1.16 \text{ eV}$, intensity ratio = 0.511). A FWHM of $\sim 1.1 \text{ eV}$ was applied for the sulfur species. To minimize air exposure, all samples were transferred from a glove box via an argon-filled vessel to the analysis chamber. UV-vis spectroscopy on the redox between PTO and $\text{Li}_6\text{PS}_5\text{Cl}$ was conducted in a CH_3CN -ethanol mixed solvent (11:1, v/v). Briefly, 200 μL $\text{Li}_6\text{PS}_5\text{Cl}$ /ethanol solution (0.8 mg mL^{-1}) was added into 2,200 μL PTO/ CH_3CN solution (0.036 mg mL^{-1}). The molar ratio of PTO: $\text{Li}_6\text{PS}_5\text{Cl}$ for reaction is 1:2.

ToF-SIMS analysis was performed using a TOF-SIMS NCS instrument, which combines a TOF SIMS instrument (ION-TOF GmbH, Münster, Germany) and an *in situ* scanning probe microscope (NanoScan, Switzerland) at Shared Equipment Authority from Rice University. 3D analysis of cycled cathodes by ToF-SIMS was conducted by using Bi_3^+ (30 keV) as the primary probe in positive polarization mode for analysis and Cs^+ (2 keV) for sputtering. The analysis area ($60 \times 60 \mu\text{m}^2$) with a measured current of 0.2 pA was placed in the center of the sputter crater ($300 \times 300 \mu\text{m}^2$) with a typical current around 125 nA. The beams were operated in non-interlaced mode, alternating 2 analysis cycles and 20 sputtering cycles (corresponding to 31.67 s) followed by a pause of 5 s for the charge compensation with an electron flood gun. An adjustment of the charge effects has been operated using a surface potential. During depth profiling, the cycle time was fixed to 100 μs (corresponding to $m/z = 0\text{--}839$ a.m.u mass range).

Positive and negative mode of high mass resolution spectra of the control samples were performed using a TOF-SIMS NCS instrument. A bunched 30 keV Bi_3^+ ions (with a measured current of 0.2 pA) was used as the primary probe for analysis (scanned area $100 \times 100 \mu\text{m}^2$) with a raster of 128×128 pixels. A charge compensation with an electron flood gun has been applied during the analysis. An adjustment of the charge effects has been operated using appropriate surface potential and extraction bias for the positive and negative polarity. The cycle time was fixed to 90 μs (corresponding to $m/z = 0\text{--}737$ a.m.u mass range). The mass spectra were acquired after a 20–30 min sputtering using a cesium ion beam at 2 keV with 105 nA. To minimize air exposure, all samples were transferred from an argon-filled vessel to the analysis chamber.

Electrochemical measurements

All electrochemical tests were conducted at 60°C. All solid-state cell modules were tightened with an initial stack pressure of ~14 MPa calibrated from a force sensor (Autoda, AT8106-10KN). Galvanostatic discharge-charge profiles were recorded with a battery tester (LAND CT-2001A) within a voltage range of 1.5–3.5 V versus Li⁺/Li. The reversible capacity values of the 3rd cycle were used for the calculation of PTO utilization. The galvanostatic intermittent potential profiles coupled with electrochemical impedance spectroscopy were recorded on an electrochemical workstation (VMP3, Bio-Logic). The current was maintained at 0.1C (1C= 409 mA g⁻¹) and the cells rest for 0.5 h prior to each EIS measurement.

E_{CAM} and $E_{Electrode}$ are calculated by integrating voltage over discharge capacity:

$E_{CAM} = \int V dC_S$, $E_{Electrode} = E_{CAM} \times f_{CAM}$, where V is the discharge voltage, and C_S is specific capacity. For a fair comparison with LMOs, Li₄PTO (370 mAh g⁻¹) instead of PTO (409 mAh g⁻¹) was employed in E_{CAM} and $E_{Electrode}$ calculation.

SUPPLEMENTAL INFORMATION

Supplemental information can be found online at <https://doi.org/10.1016/j.joule.2021.05.017>.

ACKNOWLEDGMENTS

This work was mainly supported by the U.S. Department of Energy's Office of Energy Efficiency and Renewable Energy (EERE), as part of the Battery 500 Consortium under contract DE-EE0008234. The work on interphase characterization was supported by the U.S. Department of Energy's Office of Energy Efficiency and Renewable Energy (EERE) under the Vehicle Technologies Program under contract DE-EE0008864. ToF-SIMS analysis was carried out with support provided by the National Science Foundation CBET-1626418. This work was conducted in part using resources of the Shared Equipment Authority at Rice University.

AUTHOR CONTRIBUTIONS

J.Z. and Y.Y. conceived this work. Y.Y. obtained funding and supervised the project. J.Z., Z.C., Y.L., and Y.Y. contributed to the design of experiments. J.Z. first demonstrated the solvent-mixing method and Z.C. contributed to optimizations. F.H., Z.C., and J.Z. synthesized the materials. J.Z. and Z.C. carried out the electrochemical measurements. Q.A., H.G., and J.L. performed the FIB-SEM measurements. Z.C., Q.A., and T.T. performed microscopic and TOF-SIMS analysis. J.Z., Z.C., Y.L., and Y.Y. wrote the paper. All authors analyzed the results and commented on the manuscript.

DECLARATION OF INTERESTS

Y.Y. and Y.L. have equity interest in LiBeyond LLC. Their relationship with LiBeyond LLC has been reviewed and approved by the University of Houston in accordance with its conflict of interest policies.

Received: October 15, 2020

Revised: November 23, 2020

Accepted: May 19, 2021

Published: June 17, 2021

REFERENCES

- Manthiram, A., Yu, X.W., and Wang, S.F. (2017). Lithium battery chemistries enabled by solid-state electrolytes. *Nat. Rev. Mater.* 2, 16103.
- Randau, S., Weber, D.A., Kötz, O., Koerver, R., Braun, P., Weber, A., Ivers-Tiffée, E., Adermann, T., Kulisich, J., Zeier, W.G., et al. (2020). Benchmarking the performance of all-solid-state lithium batteries. *Nat. Energy* 5, 259–270.
- Zhao, Q., Stalin, S., Zhao, C.Z., and Archer, L.A. (2020). Designing solid-state electrolytes for safe, energy-dense batteries. *Nat. Rev. Mater.* 5, 229–252.
- Zheng, F., Kotobuki, M., Song, S.F., Lai, M.O., and Lu, L. (2018). Review on solid electrolytes for all-solid-state lithium-ion batteries. *J. Power Sources* 389, 198–213.
- Wang, C.W., Fu, K., Kammampata, S.P., McOwen, D.W., Samson, A.J., Zhang, L., Hitz, G.T., Nolan, A.M., Wachsmann, E.D., Mo, Y., et al. (2020). Garnet-type solid-state electrolytes: materials, interfaces, and batteries. *Chem. Rev.* 120, 4257–4300.
- Li, X.N., Liang, J., Yang, X., Adair, K.R., Wang, C., Zhao, F., and Sun, X. (2020). Progress and perspectives on halide lithium conductors for all-solid-state lithium batteries. *Energy Environ. Sci.* 13, 1429–1461.
- Kato, Y., Hori, S., Saito, T., Suzuki, K., Hirayama, M., Mitsui, A., Yonemura, M., Iba, H., and Kanno, R. (2016). High-power all-solid-state batteries using sulfide superionic conductors. *Nat. Energy* 1, 16030.
- Miura, A., Rosero-Navarro, N.C., Sakuda, A., Tadanaga, K., Phuc, N.H.H., Matsuda, A., Machida, N., Hayashi, A., and Tatsumisago, M. (2019). Liquid-phase syntheses of sulfide electrolytes for all-solid-state lithium battery. *Nat. Rev. Chem.* 3, 189–198.
- Gao, Y., Wang, D., Li, Y.C., Yu, Z., Mallouk, T.E., and Wang, D. (2018). Salt-based organic-inorganic nanocomposites: towards a stable lithium metal/Li10GeP2S12 solid electrolyte interface. *Angew. Chem. Int. Ed.* 57, 13608–13612.
- Wu, J.H., Liu, S.F., Han, F.D., Yao, X.Y., and Wang, C.S. (2021). Lithium/sulfide all-solid-state batteries using sulfide electrolytes. *Adv. Mater.* 33, e2000751.
- Hao, F., Han, F.D., Liang, Y.L., Wang, C.S., and Yao, Y. (2018). Architectural design and fabrication approaches for solid-state batteries. *MRS Bull.* 43, 775–781.
- Choi, H.U., Jin, J.S., Park, J.Y., and Lim, H.T. (2017). Performance improvement of all-solid-state Li-S batteries with optimizing morphology and structure of sulfur composite electrode. *J. Alloys Compd.* 723, 787–794.
- Han, F.D., Yue, J., Fan, X., Gao, T., Luo, C., Ma, Z., Suo, L., and Wang, C. (2016). High-performance all-solid-state lithium-sulfur battery enabled by a mixed-conductive Li2S nanocomposite. *Nano Lett.* 16, 4521–4527.
- Choi, S.J., Choi, S.H., Bui, A.D., Lee, Y.J., Lee, S.M., Shin, H.C., and Ha, Y.C. (2018). LiI-doped sulfide solid electrolyte: enabling a high-capacity slurry-cast electrode by low-temperature post-sintering for practical all-solid-state lithium batteries. *ACS Appl. Mater. Interfaces* 10, 31404–31412.
- Zhang, Q., Cao, D., Ma, Y., Natan, A., Aurora, P., and Zhu, H. (2019). Sulfide-based solid-state electrolytes: synthesis, stability, and potential for all-solid-state batteries. *Adv. Mater.* 31, e1901131.
- Park, J., Kim, K.T., Oh, D.Y., Jin, D., Kim, D., Jung, Y.S., and Lee, Y.M. (2020). Digital twin-driven all-solid-state battery: unraveling the physical and electrochemical behaviors. *Adv. Energy Mater.* 10, 2001563.
- Strauss, F., Bartsch, T., de Biasi, L., Kim, A., Janek, J., Hartmann, P., and Brezesinski, T. (2018). Impact of cathode material particle size on the capacity of bulk-type all-solid-state batteries. *ACS Energy Lett.* 3, 992–996.
- Shi, T., Tu, Q., Tian, Y., Xiao, Y., Miara, L.J., Kononova, O., and Ceder, G. (2020). High active material loading in all-solid-state battery electrode via particle size optimization. *Adv. Energy Mater.* 10, 1902881.
- Bielefeld, A., Weber, D.A., and Janek, J. (2019). Microstructural modeling of composite cathodes for all-solid-state batteries. *J. Phys. Chem. C* 123, 1626–1634.
- Lee, Y.G., Fujiki, S., Jung, C., Suzuki, N., Yashiro, N., Omoda, R., Ko, D., Shiratsuchi, T., Sugimoto, T., Ryu, S., et al. (2020). High-energy long-cycling all-solid-state lithium metal batteries enabled by silver-carbon composite anodes. *Nat. Energy* 5, 299–308.
- Liang, Y.L., and Yao, Y. (2018). Positioning organic electrode materials in the battery landscape. *Joule* 2, 1690–1706.
- Poizot, P., Gaubicher, J., Renault, S., Dubois, L., Liang, Y., and Yao, Y. (2020). Opportunities and challenges for organic electrodes in electrochemical energy storage. *Chem. Rev.* 120, 6490–6557.
- Hao, F., Chi, X., Liang, Y., Zhang, Y., Xu, R., Guo, H., Terlier, T., Dong, H., Zhao, K., Lou, J., and Yan, Y. (2019). Taming active material-solid electrolyte interfaces with organic cathode for all-solid-state batteries. *Joule* 3, 1349–1359.
- Chi, X.W., Liang, Y., Hao, F., Zhang, Y., Whiteley, J., Dong, H., Hu, P., Lee, S., and Yao, Y. (2018). Tailored organic electrode material compatible with sulfide electrolyte for stable all-solid-state sodium batteries. *Angew. Chem. Int. Ed. Engl.* 57, 2630–2634.
- Luo, C., Ji, X., Chen, J., Gaskell, K.J., He, X., Liang, Y., Jiang, J., and Wang, C. (2018). Solid-state electrolyte anchored with a carboxylated azo compound for all-solid-state lithium batteries. *Angew. Chem. Int. Ed. Engl.* 57, 8567–8571.
- Hao, F., Liang, Y., Zhang, Y., Chen, Z., Zhang, J., Ai, Q., Guo, H., Fan, Z., Lou, J., and Yao, Y. (2021). High-energy all-solid-state organic-lithium batteries based on ceramic electrolytes. *ACS Energy Lett.* 6, 201–207.
- Yubuchi, S., Teragawa, S., Aso, K., Tadanaga, K., Hayashi, A., and Tatsumisago, M. (2015). Preparation of high lithium-ion conducting Li6PS5Cl solid electrolyte from ethanol solution for all-solid-state lithium batteries. *J. Power Sources* 293, 941–945.
- Liu, Z.C., Fu, W., Payzant, E.A., Yu, X., Wu, Z., Dudney, N.J., Kiggans, J., Hong, K., Rondinone, A.J., and Liang, C. (2013). Anomalous high ionic conductivity of nanoporous beta-Li3PS4. *J. Am. Chem. Soc.* 135, 975–978.
- Koerver, R., Walther, F., Aygün, I., Sann, J., Dietrich, C., Zeier, W.G., and Janek, J. (2017). Redox-active cathode interphases in solid-state batteries. *J. Mater. Chem. A* 5, 22750–22760.
- Tan, D.H.S., Wu, E.A., Nguyen, H., Chen, Z., Marple, M.A.T., Doux, J., Wang, X., Yang, H., Banerjee, A., and Meng, Y.S. (2019). Elucidating reversible electrochemical redox of Li6PS5Cl solid electrolyte. *ACS Energy Lett.* 4, 2418–2427.
- Auvergniot, J., Cassel, A., Foix, D., Viallet, V., Seznec, V., and Dedryvère, R. (2017). Redox activity of argyrodite Li6PS5Cl electrolyte in all-solid-state Li-ion battery: an XPS study. *Solid State Ionics* 300, 78–85.
- Ruhl, J., Riegger, L.M., Ghidui, M., and Zeier, W.G. (2021). Impact of solvent treatment of the superionic argyrodite Li6PS5Cl on solid-state battery performance. *Adv. Energy Sustain. Res.* 2, 2000077.
- Auvergniot, J., Cassel, A., Ledeuil, J., Viallet, V., Seznec, V., and Dedryvère, R. (2017). Interface stability of argyrodite Li6PS5Cl toward LiCoO2, LiNi1/3Co1/3Mn1/3O2, and LiMn2O4 in bulk all-solid-state batteries. *Chem. Mater.* 29, 3883–3890.
- Dewald, G.F., Ohno, S., Kraft, M.A., Koerver, R., Till, P., Vargas-Barbosa, N.M., Janek, J., and Zeier, W.G. (2019). Experimental assessment of the practical oxidative stability of lithium thiophosphate solid electrolytes. *Chem. Mater.* 31, 8328–8337.
- Walther, F., Koerver, R., Fuchs, T., Ohno, S., Sann, J., Rohnke, M., Zeier, W.G., and Janek, J. (2019). Visualization of the interfacial decomposition of composite cathodes in argyrodite-based all-solid-state batteries using time-of-flight secondary-ion mass spectrometry. *Chem. Mater.* 31, 3745–3755.
- Swamy, T., Chen, X.W., and Chiang, Y.M. (2019). Electrochemical redox behavior of Li ion conducting sulfide solid electrolytes. *Chem. Mater.* 31, 707–713.
- Schwietert, T.K., Arszewska, V.A., Wang, C., Yu, C., Vasileiadis, A., de Klerk, N.J.J., Hageman, J., Hupfer, T., Kerkamm, I., Xu, Y., et al. (2020). Clarifying the relationship between redox activity and electrochemical stability in solid electrolytes. *Nat. Mater.* 19, 428–435.
- Neumann, A., Randau, S., Becker-Steinberger, K., Danner, T., Hein, S., Ning, Z., Marrow, J., Richter, F.H., Janek, J., and Latz, A. (2020). Analysis of interfacial effects in all-solid-state batteries with thiophosphate solid electrolytes. *ACS Appl. Mater. Interfaces* 12, 9277–9291.

39. Ates, T., Keller, M., Kulisch, J., Adermann, T., and Passerini, S. (2019). Development of an all-solid-state lithium battery by slurry-coating procedures using a sulfidic electrolyte. *Energy Storage Mater* 17, 204–210.
40. Kraft, M.A., et al. (2018). Inducing high ionic conductivity in the lithium superionic argyrodites $\text{Li}_{6+x}\text{P}_{(1-x)}\text{Ge}_x\text{S}_5$ for all-solid-state batteries. *J. Am. Chem. Soc.* 140, 16330–16339. <https://pubs.acs.org/doi/10.1021/jacs.8b10282>.
41. Ohtomo, T., Hayashi, A., Tatsumisago, M., Tsuchida, Y., Hama, S., and Kawamoto, K. (2013). All-solid-state lithium secondary batteries using the $75\text{Li}(2)\text{S}$ center dot $25\text{P}(2)\text{S}(5)$ glass and the $70\text{Li}(2)\text{S}$ center dot $30\text{P}(2)\text{S}(5)$ glass-ceramic as solid electrolytes. *J. Power Sources* 233, 231–235.
42. Li, Y.J., Wang, X., Zhou, H., Xing, X., Banerjee, A., Holoubek, J., Liu, H., Meng, Y.S., and Liu, P. (2020). Thin solid electrolyte layers enabled by nanoscopic polymer binding. *ACS Energy Lett* 5, 955–961.

Joule, Volume 5

Supplemental information

**Microstructure engineering of solid-state
composite cathode via solvent-assisted processing**

Jibo Zhang, Zhaoyang Chen, Qing Ai, Tanguy Terlier, Fang Hao, Yanliang Liang, Hua Guo, Jun Lou, and Yan Yao

Supplemental figures

- Figure S1.** Electrochemical performance of the Li/Li₃PS₄/Li cell.
- Figure S2.** Reversible PTO-Li₆PS₅Cl interphase in dry-mixed cathode ($f_{\text{PTO}} = 20 \text{ wt\%}$).
- Figure S3.** Reversible PTO-Li₆PS₅Cl interphase in dry-mixed cathode ($f_{\text{PTO}} = 40 \text{ wt\%}$).
- Figure S4.** Illustration of the intrinsic oxidizing strength of PTO and formation of Li_xPTO.
- Figure S5.** XPS spectra of dry-mixed cathode under different potentials.
- Figure S6.** SEM characterizations of PTO cathodes.
- Figure S7.** ToF-SIMS spectral analysis on the electrolyte species.
- Figure S8.** ToF-SIMS secondary ions (SI) images of characteristic fragments from dry-mixed and solvent-mixed cathodes ($f_{\text{PTO}} = 50 \text{ wt\%}$) during depth-profiling.
- Figure S9.** ToF-SIMS SI images of characteristic fragments from dry-mixed and solvent-mixed control samples (no conductive carbon) during depth-profiling.
- Figure S10.** ToF-SIMS spectral analysis of the dry-mixed/ solvent-mixed cathodes and control samples.
- Figure S11.** 3D distribution of the cathode components based on ToF-SIMS data.
- Figure S12.** Calculation of Warburg coefficients of solvent-mixed cathode. ($f_{\text{PTO}} = 40 \text{ wt\%}$).
- Figure S13.** XPS spectra of dry and solvent-mixed cathode in P 2p and Cl 2p region.
- Figure S14.** XPS analysis of charged and discharge cathodes.
- Figure S15.** Proposed mechanism on the evolution of interphase.
- Figure S16.** Electrochemical performance of the Li₆PS₅Cl-C composite.
- Figure S17.** 1st cycle galvanostatic potential profiles of solvent-mixed cathode ($f_{\text{PTO}} = 40 \text{ wt\%}$). And Multiple cell results at different f_{PTO} .
- Figure S18.** Battery performance with higher mass loading (10 mg).

Supplemental scheme

- Scheme S1.** Schematic illustration on the redox process in a composite cathode.

Supplemental tables

- Table S1.** Comparison of battery performance with different CAMs using lithium thiophosphates electrolytes.
- Table S2.** ToF-SIMS data summary for the fragments.
- Table S3.** The Warburg coefficients of solvent-mixed cathode ($f_{\text{PTO}} = 40 \text{ wt\%}$).
- Table S4.** Equivalent circuit and fitting parameters for the EIS Spectra of dry-mixed and solvent-mixed PTO cathodes ($f_{\text{PTO}} = 40 \text{ wt\%}$).
- Table S5.** Summary of estimated volume fraction of cathode components and volumetric energy density of PTO electrodes

Supplemental Notes

- Note S1.** Detailed analysis on the UV-Vis identification of Li_xPTO.
- Note S2.** Detailed analysis on the multiple interfaces that may undergo electrochemical process within cathode.
- Note S3.** Detailed analysis on the cathode capacity contributed by different components.

Supplemental figures

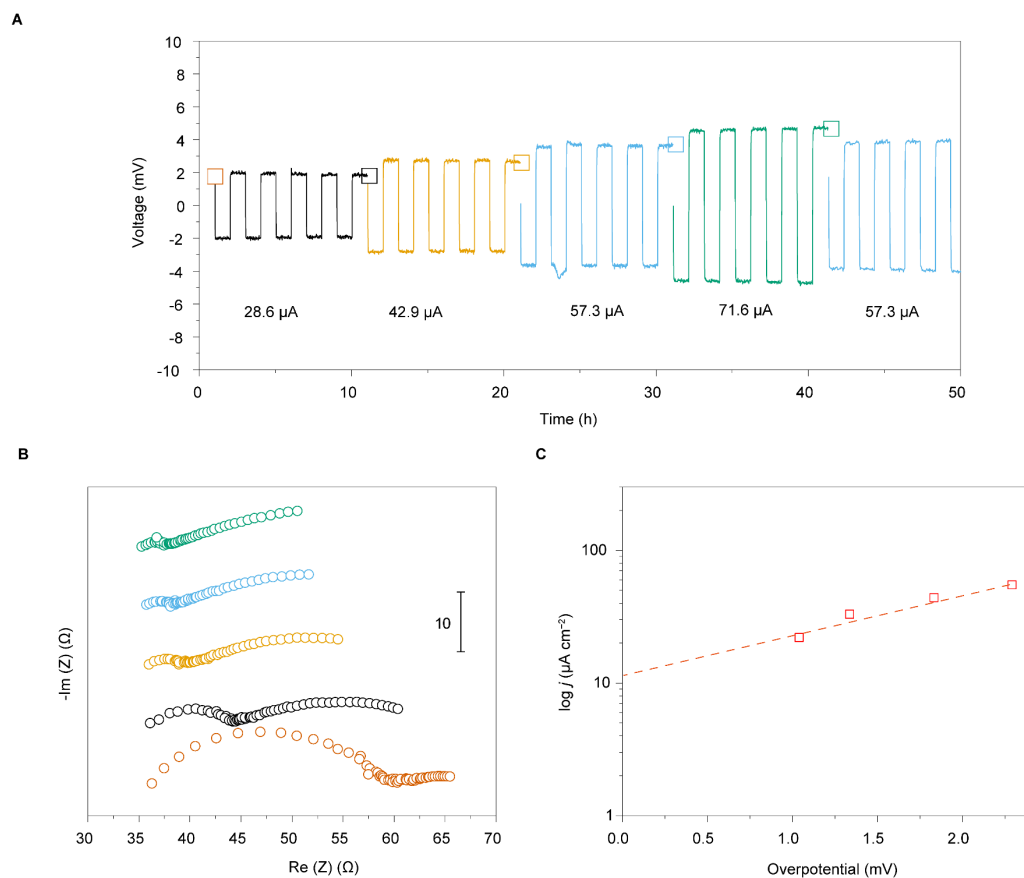


Figure S1. Electrochemical performance of a Li/Li₃PS₄/Li cell at current of 28.6 μA, 42.9 μA, 57.3 μA and 71.6 μA at 60 °C, corresponding to the equivalent cathodic current of cathode with 20-50 wt% PTO: 22, 33, 44 and 55 μA cm⁻². The electrode area is 1.3 cm². (A) Voltage vs time profile of the cell under galvanostatic Li plating/stripping. (B) EIS spectra recorded at each step. (C) Exchange current density of Li plating/stripping with Li₃PS₄ electrolyte interface of 11 μA cm⁻² under our experimental conditions.

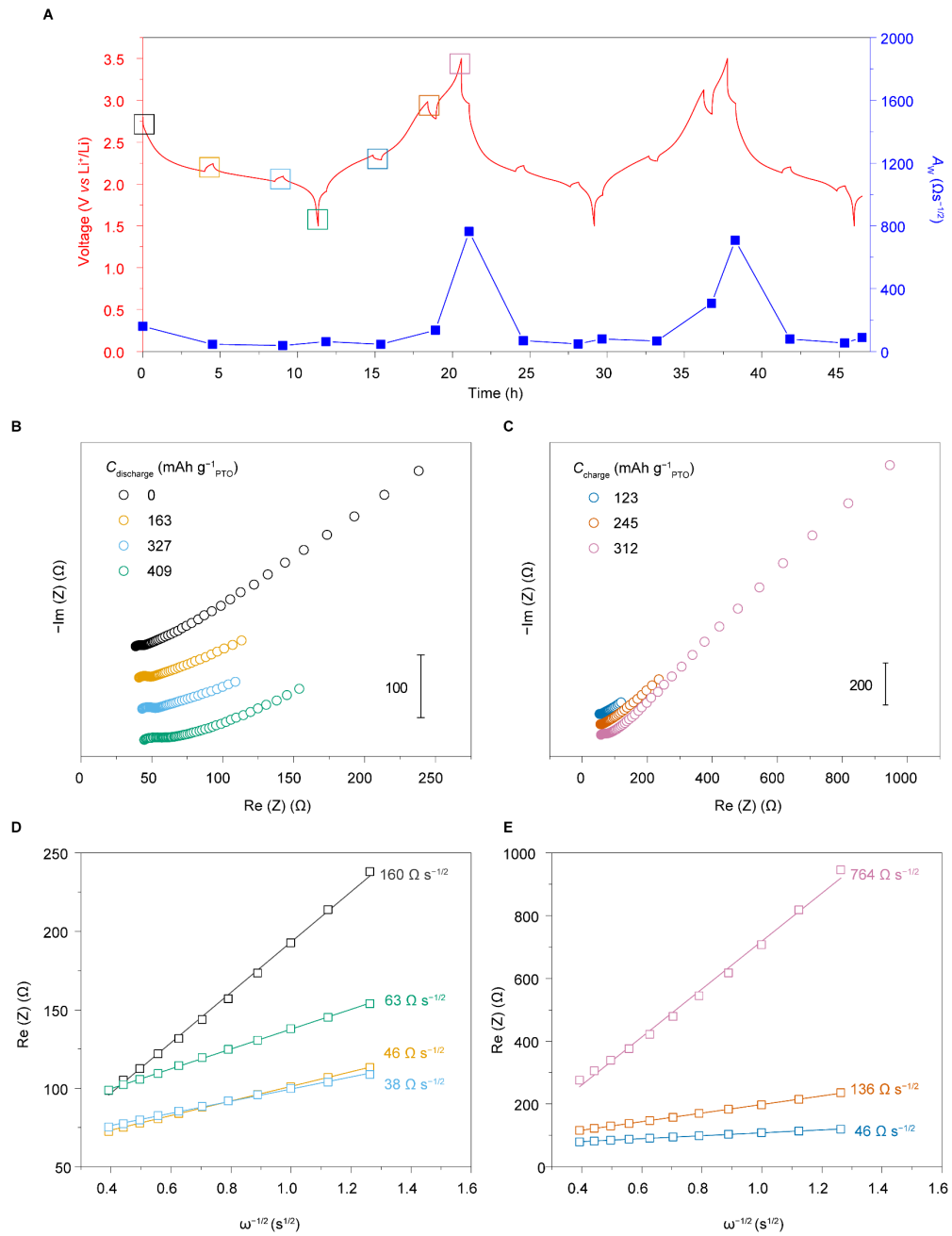


Figure S2. Reversible PTO-Li₆PS₅Cl interphase in dry-mixed cathode ($f_{\text{PTO}} = 20$ wt%). (A) Intermittent galvanostatic potential profile at 0.1C, 60 °C, and the corresponding A_W calculated from EIS data. Impedance spectra and corresponding $\text{Re}(Z)$ vs $\omega^{-1/2}$ plots for calculating A_W during (B, D) the first discharging and (C, E) the first charging.

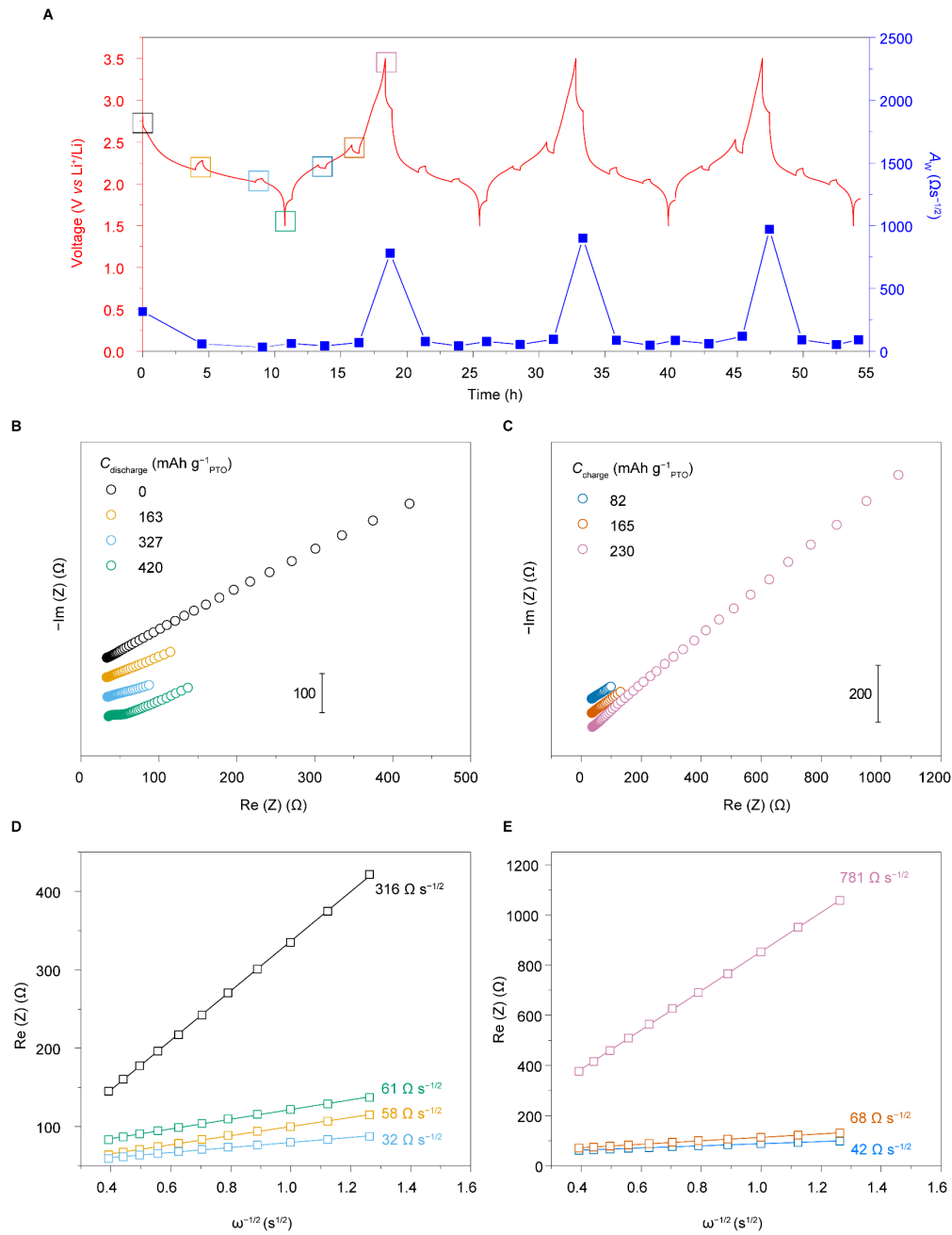


Figure S3. Reversible PTO-Li₆PS₅Cl interphase in dry-mixed cathode ($f_{PTO} = 40$ wt%). (A) Intermittent galvanostatic potential profile at 0.1C, 60 °C, and the corresponding A_W calculated from EIS data. Impedance spectra and corresponding $Re(Z)$ vs $\omega^{-1/2}$ plots for calculating A_W during (B, D) the first discharging and (C, E) the first charging.

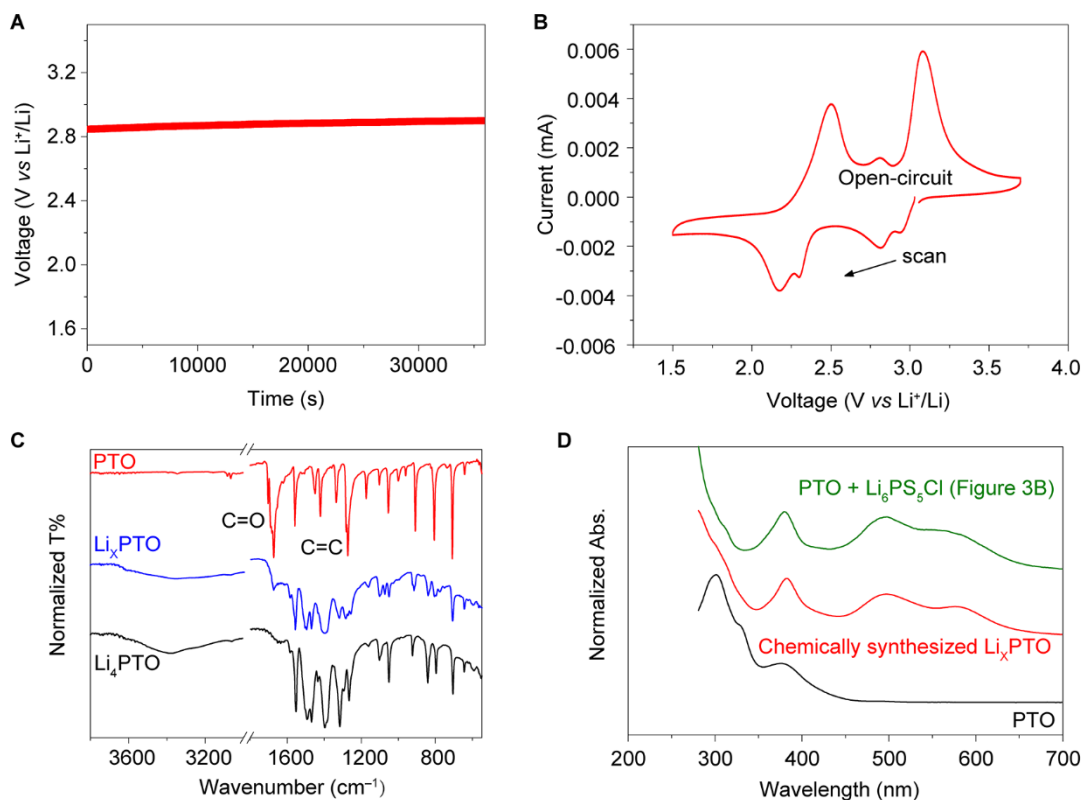


Figure S4. Illustration of the intrinsic oxidizing strength of PTO and formation of Li_xPTO . (A) The open-circuit voltage (OCV) of the $\text{Li}_6\text{PS}_5\text{Cl}$ -free PTO cathode is presented. (B) CV curve of PTO in 0.1 M LiTFSI/tetraglyme. Working electrode: glossy carbon. Reference electrode: Li metal. Counter electrode: Li metal. (C) FTIR spectroscopy showing the evolution of carbonyls in PTO, Li_xPTO and Li_4PTO . (D) Comparison of the UV-Vis spectra of PTO, chemically synthesized Li_xPTO and Li_xPTO generated by spontaneous redox (Figure 3B). A cut-off wavelength at 280 nm is applied to avoid possible interference from solvent and cuvette.

Figure S4 demonstrates the intrinsic oxidizing strength of PTO in a solid-state cell. In order to avoid the interference from the reaction between PTO and $\text{Li}_6\text{PS}_5\text{Cl}$ in a solid-state cathode, a $\text{Li}_6\text{PS}_5\text{Cl}$ -free PTO cathode was used to assemble the cell. The cell was rest at OCV, which stabilized at ~ 2.90 V (vs Li^+/Li), showing the high oxidizing strength of PTO in the solid-state electrode. The equilibrium redox potential of PTO (first electron reduction) exceeds the stability window of $\text{Li}_6\text{PS}_5\text{Cl}$ (~ 2.35 V vs Li^+/Li) and will induce interfacial redox.¹ The oxidizing strength of PTO favors the formation of lithium polythiophosphates (Li-PS_n) that contains bridging sulfur moieties ($-\text{[S]}_n^-$).² It should be noticed that the partially reduced PTO (Li_xPTO) shows a decreased equilibrium redox potential of ~ 2.5 V (vs Li^+/Li) within the stability window of $\text{Li}_6\text{PS}_5\text{Cl}$.^{1,3} Therefore, as the surface of PTO is covered by the interphase consisting of Li_xPTO and Li-PS_n , further redox reactions with $\text{Li}_6\text{PS}_5\text{Cl}$ is not sustained, and a characteristic PTO-interphase- $\text{Li}_6\text{PS}_5\text{Cl}$ structure is formed. A detailed discussion on the UV-Vis analysis is summarized in supplemental note S1.

The influence from the PTO- $\text{Li}_6\text{PS}_5\text{Cl}$ interphase at different f_{PTO} (20 and 40 wt%) was investigated by *operando* EIS (**Figure S2-3**). The A_W obtained from the EIS are used to evaluate the Li^+ diffusivity at the PTO- $\text{Li}_6\text{PS}_5\text{Cl}$ interphase.^{4,5} The capacity-potential-dependent A_W values indicate the dynamic

evolution of the interphase being consistent with the electrochemistry of PTO and lithium thiophosphates. The A_w values remained $<100 \Omega \text{ s}^{-1/2}$ within the plateau region (1.9-2.5 V vs Li^+/Li), however, increased rapidly towards the end of charge potential (3.5 V vs Li^+/Li). The latter originates from the partial decomposition of $\text{Li}_6\text{PS}_5\text{Cl}$ at the potentials exceeding its thermodynamic equilibrium.^{2,6,7} Nevertheless, the moderate operating potential of PTO favors the formation of Li^+ conductive Li-PS_n without leading to the severe oxidation of $\text{Li}_6\text{PS}_5\text{Cl}$ and accumulation of highly insulating species (S and P_2S_5) that are usually observed in LMOs.^{2,6} Consequently, the PTO- $\text{Li}_6\text{PS}_5\text{Cl}$ interphase exhibits excellent reversibility and barely affect the Li^+ diffusion.⁴ However, both dry-mixed cathodes show similar behavior at the interphase regardless of the different utilizations (79.0% vs 48.9%), and do not account for the presence of electrochemically inaccessible PTO, since only the available PTO contributes to the electrochemical response.

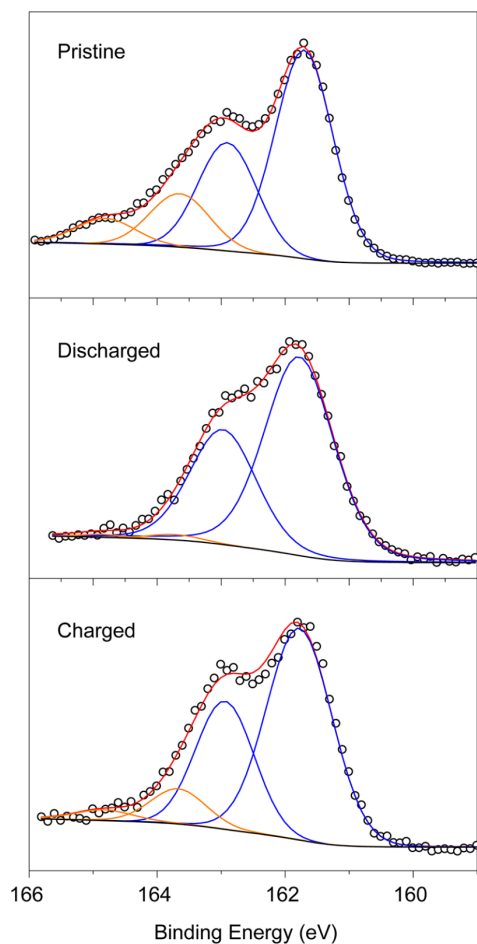


Figure S5. XPS spectra of dry-mixed cathode under different potentials.

Figure S5 shows the evolution of chemical species of the interphase in dry-mixed cathode under different potentials. Specifically, the high-resolution XPS spectra in S 2p region are fitted. The components peaking at 161.7 and 162.9 eV correspond to the $2p_{3/2}$ and $2p_{1/2}$ of sulfur in the -S-Li moieties. The oxidized $\text{Li}_6\text{PS}_5\text{Cl}$ species appear at 163.6 ($2p_{3/2}$) and 164.8 eV ($2p_{1/2}$), which are attributed to the bridging sulfur moieties ($-\text{[S]}_n^-$).^{2,7,8} The as-prepared composite cathode shows the presence of $-\text{[S]}_n^-$ due to the redox reaction between PTO and $\text{Li}_6\text{PS}_5\text{Cl}$ during the electrode preparation. The $-\text{[S]}_n^-$ were mostly reduced to -S-Li when the cathode was discharged to 1.5 V (vs Li^+/Li) along with the decrease of A_w .⁸ The -S-Li moieties were oxidized to $-\text{[S]}_n^-$ as the cathode was charged to 3.5 V (vs Li^+/Li), and accumulation of $-\text{[S]}_n^-$ species led to a rapid increase of A_w .⁸ The reversible evolution of $-\text{[S]}_n^-$ and -S-Li species accounts for the reversible A_w values shown in **Figure S2-3**.

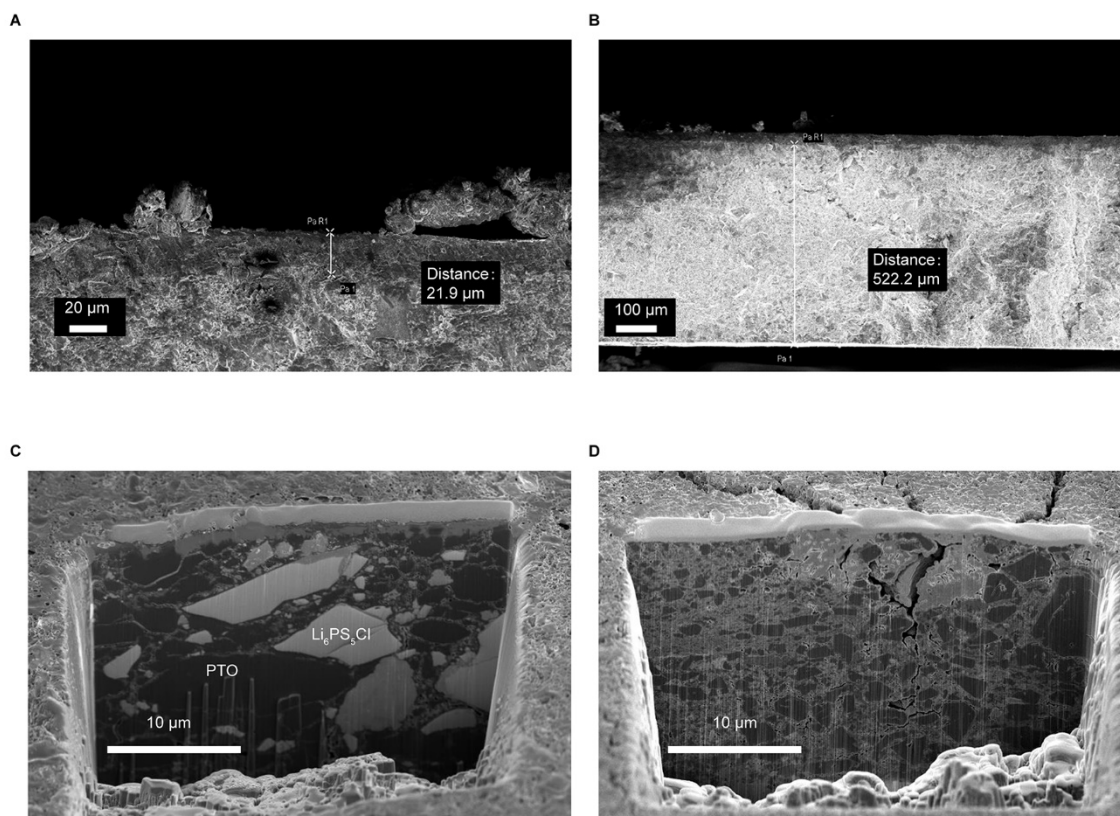


Figure S6. Characterizations of PTO cathodes. Cross-sectional SEM images of (A) a solvent-mixed PTO cathode (3.5 mg, $f_{\text{PTO}} = 40 \text{ wt}\%$) and (B) an electrolyte layer (130 mg, $\text{Li}_6\text{PS}_5\text{Cl}$). SEM images of (C) dry-mixed and (D) solvent-mixed cathodes ($f_{\text{PTO}} = 50 \text{ wt}\%$).

Figure S6A-B show the cross-sectional SEM images of a solvent-mixed cathode with the electrolyte layer. The typical thickness of a cathode is $\sim 26 \mu\text{m}$, and that of the electrolyte layer is $522 \mu\text{m}$. **Figure S6C-D** show the cross-sectional images of dry-mixed and solvent-mixed cathodes at $f_{\text{PTO}} = 50 \text{ wt}\%$.

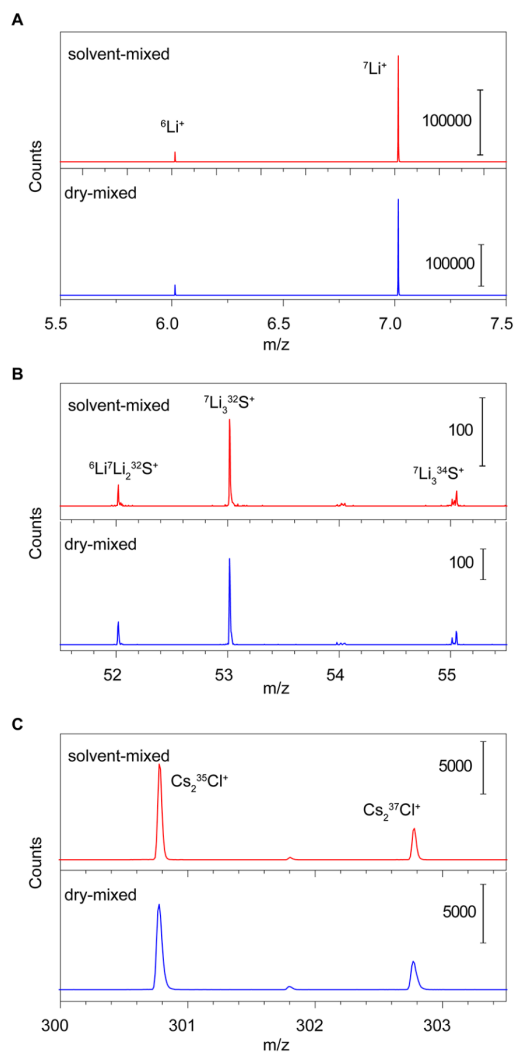


Figure S7. ToF-SIMS spectral analysis of electrolyte species. Mass spectra of specific fragments are shown: (A) Li^+ , (B) Li_3S^+ and (C) Cs_2Cl^+ . Note that the spectra used for the identification of peak with isotopes as reference, instead of a direct comparison on the peak intensities between dry- and solvent-mixed cathode.

Figure S7 shows the mass spectra collected from ToF-SIMS for several positive fragments. Since fragments would come out due to the collision between incident ions and the sample, we picked the fragments with characteristic m/z values to identify the $\text{Li}_6\text{PS}_5\text{Cl}$ -derived species. $\text{Li}_6\text{PS}_5\text{Cl}$ is Li, S and Cl rich, whereas PTO phase is C, H and O rich. Therefore, the fragments consisting of Li, S or Cl originate from the fragmentation of $\text{Li}_6\text{PS}_5\text{Cl}$. The presence of Cs is due to the sputtering process (Cs^+ ion beam) during the depth profiling. Abundance of isotopes was further evaluated to confirm the fragment identification. The relative intensities of the characteristic isotopic fragments, such as Li^+ , Li_3S^+ and Cs_2Cl^+ , match well with the natural abundance of corresponding isotopes. Please note that the $\text{Li}_6\text{PS}_5\text{Cl}$ -PTO interphase might contribute merely in the distribution of Li^+ and Li_3S^+ , because the interphase also contains Li and S species. Identification of characteristic fragments from PTO phase is discussed in **Figure S8-10**.

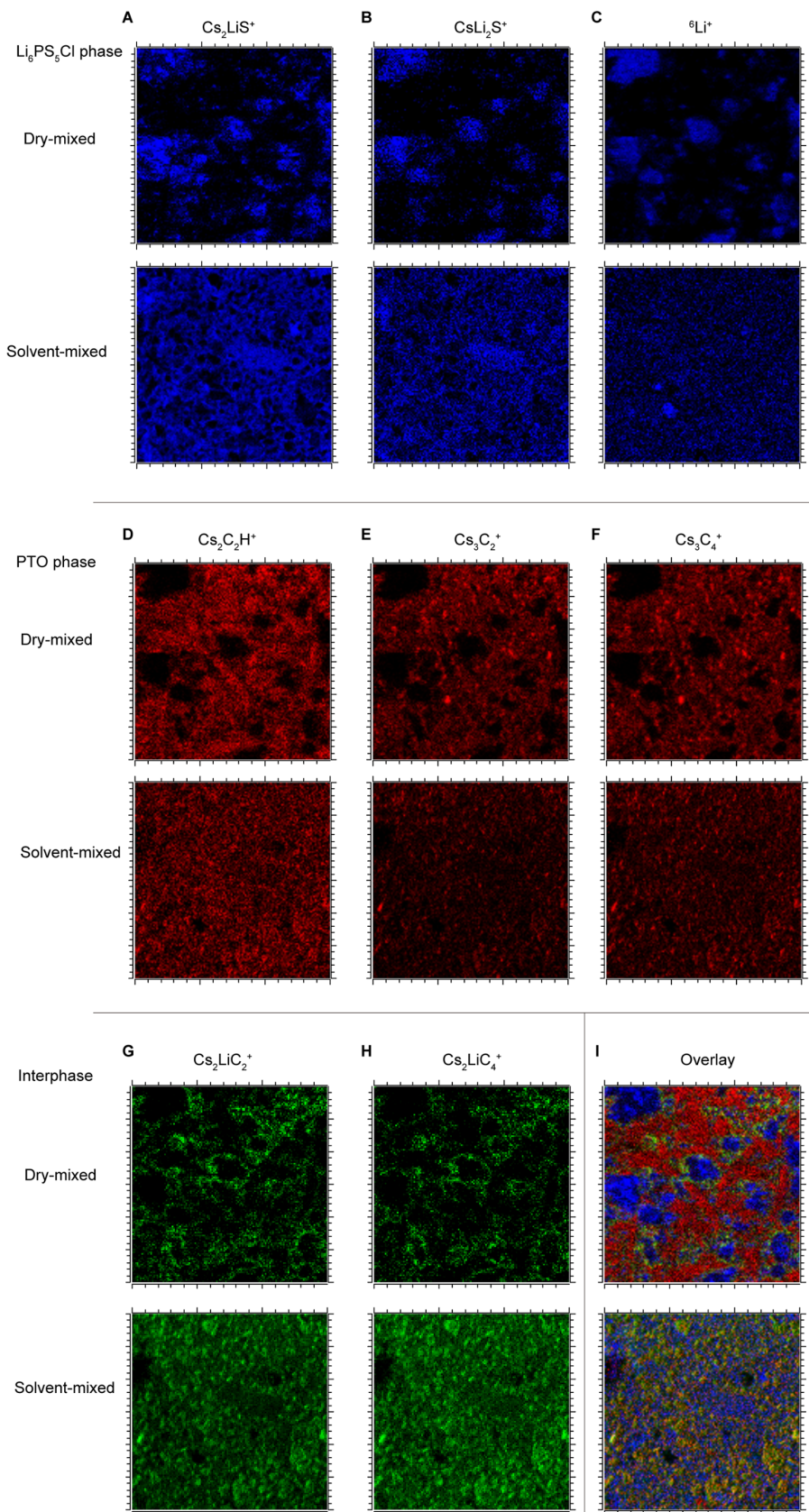


Figure S8. ToF-SIMS secondary ions (SI) images of characteristic fragments in dry-mixed and solvent-mixed cathodes ($f_{\text{PTO}} = 50 \text{ wt}\%$). The 2D images show the distribution of characteristic fragments from (A-C) $\text{Li}_6\text{PS}_5\text{Cl}$ phase, (D-F) PTO phase, (G-H) interphase, and (I) the overlay images. The image area

is $60 \times 60 \mu\text{m}^2$.

In order to identify the PTO phase and interphase, we first refer to the distribution of the characteristic fragments as recorded by ToF-SIMS. Due to sputtering by Cs^+ ion beam, the dominant fragments consist of Cs. A summary of the assignment of the fragments is provided in **Table S1**. As shown in **Figure S8**, the fragments are classified into three categories based on their spatial distribution and the local abundance of elements. For example, as previously discussed the $\text{Li}_6\text{PS}_5\text{Cl}$ is Li and S rich while C deficient, we identified the fragments derived from $\text{Li}_6\text{PS}_5\text{Cl}$ phase including (A) Cs_2LiS^+ , (B) CsLi_2S^+ and (C) ${}^6\text{Li}^+$.

The PTO phase is C-rich (PTO and conductive carbon) and therefore abundant Cs-carbon cluster ions are generated during the Cs^+ ion sputtering and fragmentation process.^{9,10} The distribution of the fragments derived from PTO phase, such as $\text{Cs}_2\text{C}_2\text{H}^+$, Cs_3C_2^+ and Cs_3C_4^+ (D-F), show clearly complementary distribution to that of $\text{Li}_6\text{PS}_5\text{Cl}$ phase. We further prepared the control samples (conductive carbon-free, **Figure S9**) to avoid the possible interference from conductive carbon.

Identification of fragments from interphase highly depends on the coherence of spatial distribution and local abundance of elements. We figured out two representative fragments, yet their chemical compositions remain indistinguishable due to the nearly identical m/z values: (G) $\text{Cs}_2\text{LiC}_2^+$ ($m/z \sim 296.8$) and (H) $\text{Cs}_2\text{LiC}_4^+$ ($m/z \sim 320.8$). The Cs-Li carbon cluster ions are likely from the fragmentation of Li_xPTO . Indeed, the only credible origin of the Li/C-containing fragments is the Li_xPTO from the interphase, which matches well with the spatial distribution in the SI images. On the other hand, since the reduction (lithiation) of PTO occurs at the carbonyls, the Li_xPTO possesses R-O-Li moieties resembling the phenolates. Therefore, the negative oxygen-containing ion fragments (CH_3O^- , $\text{C}_3\text{H}_3\text{O}^-$) may also form and cluster with Cs^+ to generate $\text{Cs}_2\text{CH}_3\text{O}^+$ and $\text{Cs}_2\text{C}_3\text{H}_3\text{O}^+$, as will be further discussed in **Figure S10**.^{11,12} Besides, the overlay images (I) show the severe phase separation in dry-mixed cathode, which is in sharp contrast to the solvent-mixed cathode with an interconnecting network.

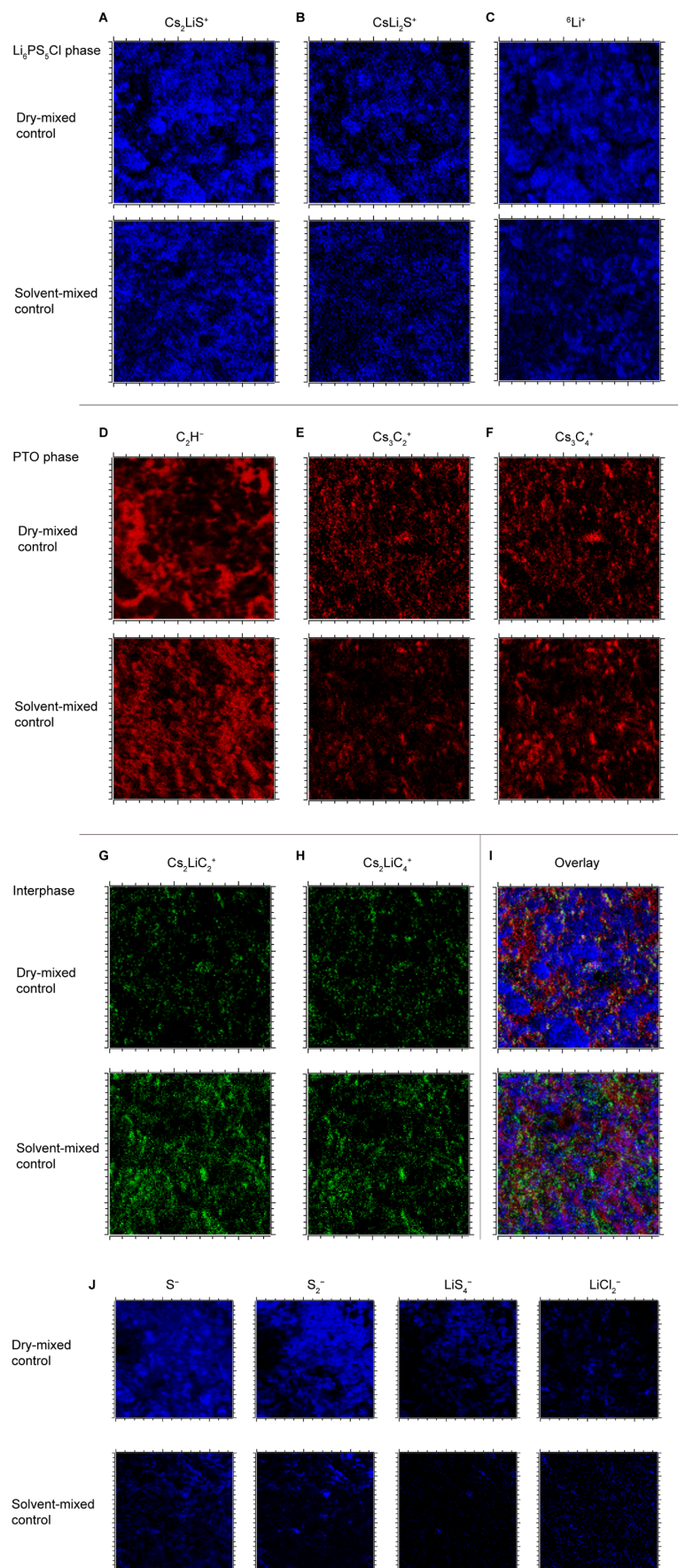


Figure S9. ToF-SIMS SI images of characteristic fragments in dry-mixed and solvent-mixed control samples (no conductive carbon) during depth-profiling. The 2D images show the distribution of characteristic fragments from (A-C) $\text{Li}_6\text{PS}_5\text{Cl}$ phase, (D-F) PTO phase, (G-H) interphase, and (I) the overlay images. (J) SI images of negatively charged species in control samples (no carbon). The image area is $60 \times 60 \mu\text{m}^2$.

To avoid the interference of conductive carbon on the fragment identification, the conductive carbon-free dry-mixed and SP control samples were prepared and characterized by ToF-SIMS as shown in **Figure S9**. Similar to the dry-mixed and solvent-mixed cathodes, the $\text{Li}_6\text{PS}_5\text{Cl}$ phase (A-C) and PTO phase (D-F) could be identified by the characteristic fragments. Both dry-mixed and SP control samples exhibit significant amount of Cs-carbon cluster ions, which originate from the fragmentation of PTO.

Although the same fragments from PTO- $\text{Li}_6\text{PS}_5\text{Cl}$ interphase, (G) $\text{Cs}_2\text{LiC}_2^+$ and (H) $\text{Cs}_2\text{LiC}_4^+$, were observed in the control samples, their intensities are relatively low compared to the dry-mixed and solvent-mixed cathodes (quantified in **Figure S10**). The results indicate that redox between PTO and $\text{Li}_6\text{PS}_5\text{Cl}$ is less sufficient in the absence of conductive carbon. And this is reasonable since carbon provides a higher contact area and a better electronic conductivity to facilitate the local redox between PTO and $\text{Li}_6\text{PS}_5\text{Cl}$. Additionally, the overlay images (I) shows the similar trend as observed in the dry-mixed and solvent-mixed cathodes. The SI images of negatively charged species (J) show similar distribution to the positively charge species. However, it is difficult to distinguish the interphase from $\text{Li}_6\text{PS}_5\text{Cl}$ or PTO phases.

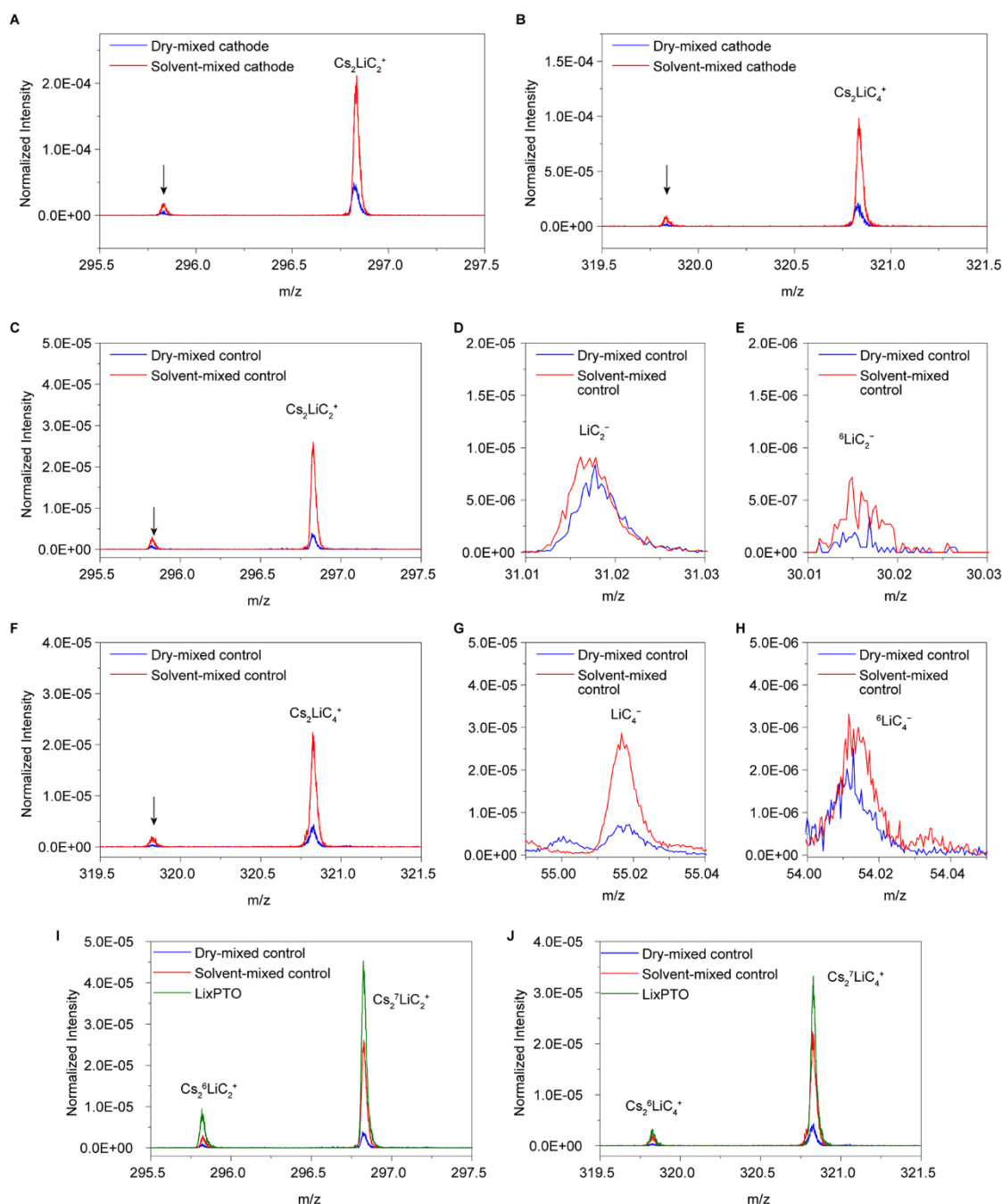


Figure S10. TOF-SIMS spectral analysis of the dry-mixed/SP cathodes and control samples. (A) $\text{Cs}_2\text{LiC}_2^+$ and (B) $\text{Cs}_2\text{LiC}_4^+$ from the dry-mixed and solvent-mixed cathodes. (C) $\text{Cs}_2\text{LiC}_2^+$ and (D, E) LiC_2^- identifications from the dry-mixed and solvent-mixed control samples. (F) $\text{Cs}_2\text{LiC}_4^+$ and (G, H) LiC_4^- identifications from the dry-mixed and solvent-mixed control samples. (I, J). ToF-SIMS spectra of chemically synthesized Li_xPTO (positive mode, Cs-sputtered) and comparison with dry and solvent-mixed samples. The intensity is normalized to total ion counts.¹³

Figure S10 provides a quantitative analysis on the fragments from the interphase in addition to images presented in **Figure S8-9**. The spectra have been normalized by their respective total ion counts. As shown in (A) and (B), due to the overlapped m/z values, the relative amount of $\text{Cs}_2\text{LiC}_2^+$ ($m/z \sim 296.8$)

and $\text{Cs}_2\text{LiC}_4^+$ ($m/z \sim 320.8$) cannot be arbitrarily determined. Additionally, the normalized intensities of $\text{Cs}_2\text{LiC}_2^+$ and $\text{Cs}_2\text{LiC}_4^+$ are around an order of magnitude lower in control samples (C, F) than in cathodes (A, B), which is due to the less sufficient redox as discussed above. However, the intensity of the fragments in solvent-mixed control is still significantly higher than that in the dry-mixed control, being consistent with the mechanism that solvent-mixed promotes a more sufficient redox between PTO and $\text{Li}_6\text{PS}_5\text{Cl}$. Since the $\text{Cs}_n\text{Li}_x\text{C}_y^+$ is from the Li_xPTO (interphase), a higher normalized intensity suggests more interphase area in the analyzed cross-section ($60 \text{ by } 60 \mu\text{m}^2$). Indeed, smaller particle size in solvent-mixed cathode indicates a higher PTO- $\text{Li}_6\text{PS}_5\text{Cl}$ interfacial area, leading to more Li_xPTO formed. As for the SI images, normalization based on region-of-interest analysis (pixel-counting method: Chem. Mater. 2019, 31, 3745-3755) is not necessary here since our focus is on microstructure instead of reaction kinetics. Furthermore, the fragments at lower m/z values ($m/z \sim 295.8$ and $m/z \sim 319.8$, indicated by arrow) with relative intensity ratio of $\sim 1:9$ suggest the isotopic species (^6Li) in these fragments. Therefore, the result suggests the presence of $\text{Cs}_2\text{LiC}_2^+$ and $\text{Cs}_2\text{LiC}_4^+$, despite the possible existence of $\text{Cs}_2\text{CH}_3\text{O}^+$ and $\text{Cs}_2\text{C}_3\text{H}_3\text{O}^+$. This hypothesis is further validated in the spectra of dry-mixed and solvent-mixed control samples (C-H), where the isotopic species (^6Li) are presented. In the control samples, we further identified the negatively charged Li-carbon clusters as: (D) LiC_2^- and (G) LiC_4^- with the isotopic fragments, respectively. These Li-carbon clusters ions could bond Cs^+ and form the $\text{Cs}_2\text{LiC}_2^+$ and $\text{Cs}_2\text{LiC}_4^+$, respectively. Although the identification of fragments from oxidized $\text{Li}_6\text{PS}_5\text{Cl}$ remains a challenge, the formation of the above cluster ions confirms the chemical composition of the PTO- $\text{Li}_6\text{PS}_5\text{Cl}$ interphase.

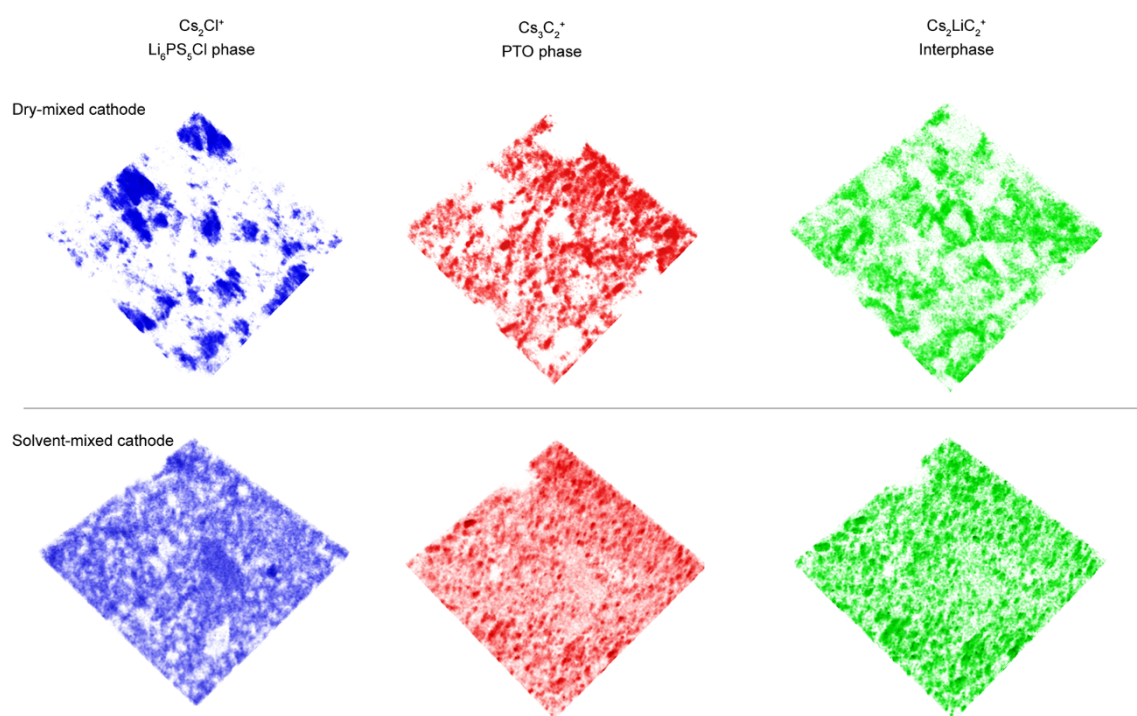


Figure S11. Spatial distribution of (a) $\text{Li}_6\text{PS}_5\text{Cl}$ (Cs_2Cl^+), (b) PTO (Cs_3C_2^+) and the interphase ($\text{Cs}_2\text{LiC}_2^+$). The area is $60 \times 60 \mu\text{m}^2$.

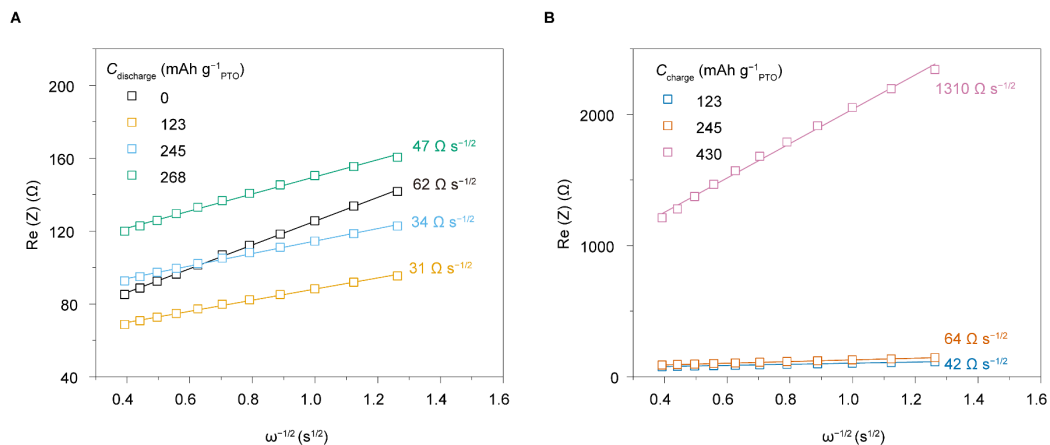


Figure S12. Calculation of A_W of solvent-mixed cathode. ($f_{PTO} = 40\ wt\%$). (A) Galvanostatic (0.1C) discharging and (B) charging process. A_W values are obtained from the slope of the $Re(Z)$ vs. $\omega^{-1/2}$ at low frequencies, and the evolution of A_W is shown in **Figure 5**.

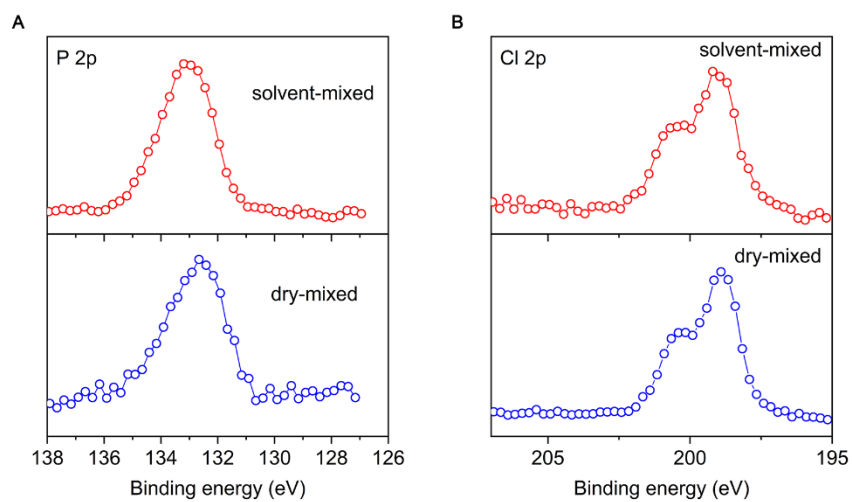


Figure S13. XPS spectra of dry and solvent-mixed cathode in (A) P 2p and (B) Cl 2p region.

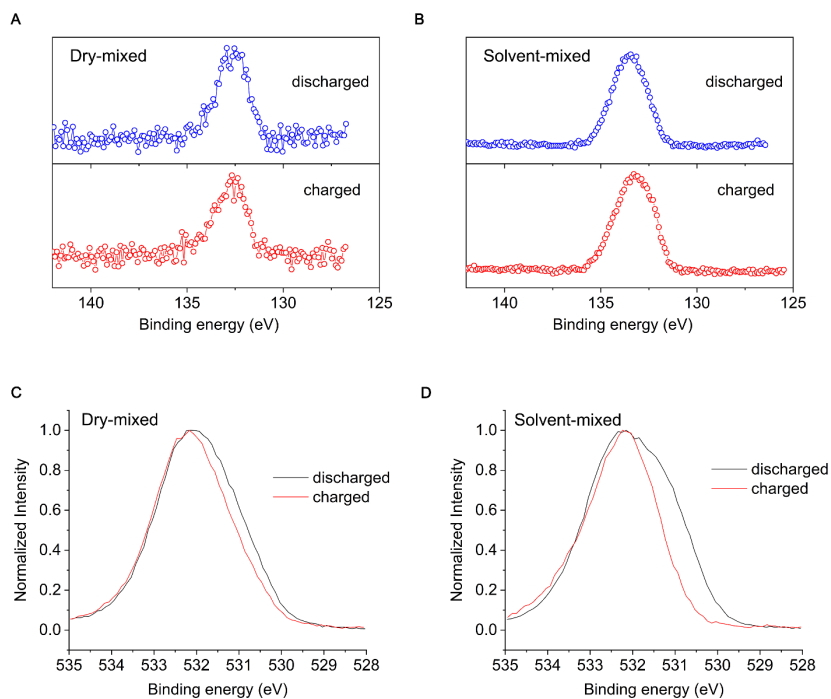


Figure S14. XPS analysis of charged and discharge cathodes. P 2p region of (A) dry-mixed and (B) solvent-mixed cathodes. O 1s region for (C) dry-mixed and (D) solvent-mixed cathodes.

In the XPS spectra in P 2p region, the slightly lower signal-to-noise ratio of dry-mixed electrode is very likely caused by its microstructure, where $\text{Li}_6\text{PS}_5\text{Cl}$ particles are coated by PTO. No substantial difference in the peaks is observed when the both cathodes are discharged and charged, confirming that the redox of thiophosphate mainly occurs at the $-\text{S-Li}$ moieties and the chemical environment of phosphorous barely changes. We characterized the spectra in O 1s region of charged and discharged samples as shown in Figure S14C-D. It should be noted that the XPS spectra only provide qualitative analysis, and the electronic delocalization effect of the conjugated backbone would lead to line-shape deformation and peak-broadening. Nevertheless, both discharged samples show an increase of intensity at lower binding energy (~ 531.5 eV), due to the formation of “lithium phenolate-like” structure after discharging. Specifically, the solvent-mixed sample shows a more obvious increase, corroborating to the electrochemical result of higher PTO utilization.

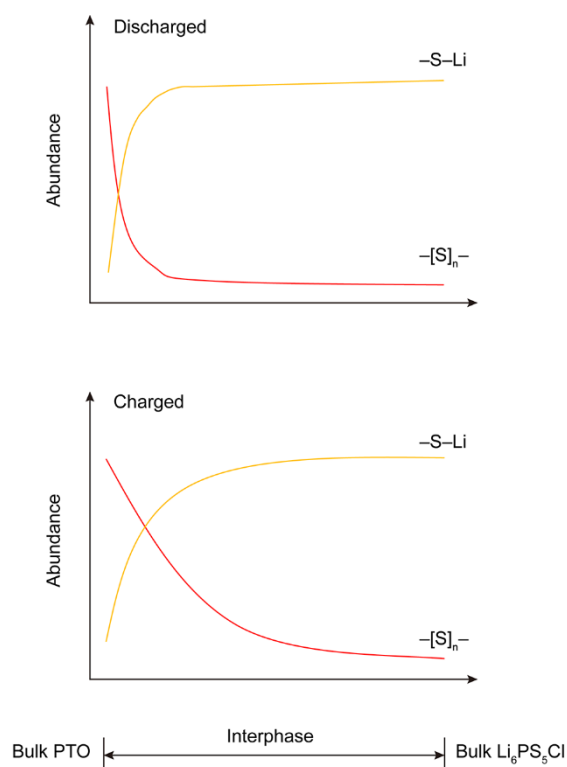


Figure S15. Proposed $\text{Li}_6\text{PS}_5\text{Cl}$ -PTO interphase on sulfur-based species.

Figure S15 illustrates the evolution of interphase. Based on the electrochemical data and XPS analysis, a potential-dependent composition mechanism is proposed. Within the working potential of PTO (1.5-3.5 V vs Li^+/Li), the redox of $\text{Li}_6\text{PS}_5\text{Cl}$ mainly transform reversibly between $-\text{S-Li}$ and $-\text{[S]}_n^-$ moieties.^{1,2,7,8,14} The relative ratio of $-\text{S-Li}$ and $-\text{[S]}_n^-$ depends on the local oxidizing strength (electron affinity). Since accumulation of $-\text{[S]}_n^-$ suppresses the Li^+ conductivity and thus lower the equivalent local potential, distribution of $-\text{[S]}_n^-$ and $-\text{S-Li}$ species would vary depending on the distance away from the bulk PTO phase. For example, under the high anodic potential (e.g. ~ 3.5 V vs Li^+/Li) during charge process, the PTO phase possesses electrostatic potential nearly equals to that of the current collector and will readily oxidize $-\text{S-Li}$ to $-\text{[S]}_n^-$. The local abundance of $-\text{[S]}_n^-$ moieties would be the highest at the PTO-interphase contact and decrease towards the bulk $\text{Li}_6\text{PS}_5\text{Cl}$ phase due to the lowered local potential. During the discharge process, the $-\text{[S]}_n^-$ is reduced to $-\text{S-Li}$ (lithiation) and the local concentration of $-\text{[S]}_n^-$ drops rapidly.² It is worth noting that the end of discharge potential (1.5 V vs Li^+/Li) is above the reducing potential of PS^{3-} and thus no reductive decomposition of $\text{Li}_6\text{PS}_5\text{Cl}$ is expected.¹⁴

Formation of the reversible interphase is available within a proper potential window. If the local electrostatic potential is high enough to further delithiate all the $-\text{S-Li}$ moieties, the highly insulating species, such as S and P_2S_5 , will accumulate at the interphase. Their relatively low e^-/Li^+ conductivity leads to poor reversibility of the interphase and rapid performance decay of the cathode. Such mechanism has been proved by CAMs with high working potentials beyond 4.0 V (LiCoO_2 and $\text{LiNi}_x\text{Mn}_y\text{Co}_z\text{O}_2$).⁶ A protection layer (with a Li^+ conductivity yet electronic insulating) on CAMs is generally necessary.¹⁵⁻¹⁷

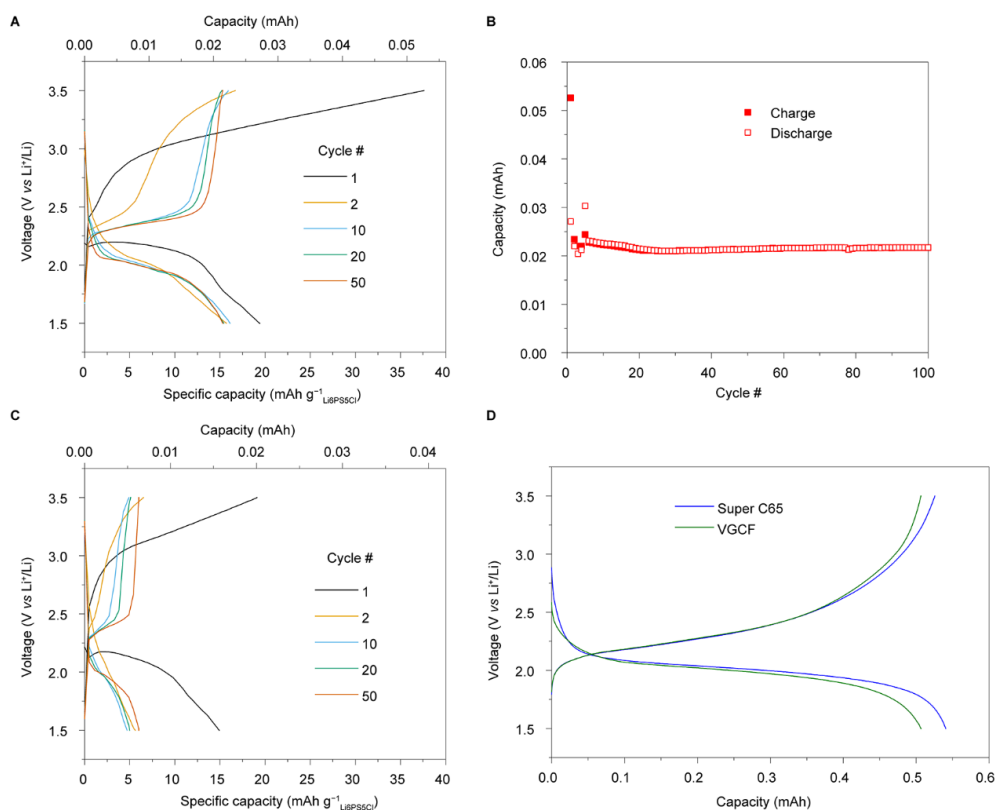


Figure S16. (A-B) Electrochemical performance of the $\text{Li}_6\text{PS}_5\text{Cl-C}$ composite (4/1 w/w, SSE/carbon). (A) Galvanostatic potential profiles of the $\text{Li}_6\text{PS}_5\text{Cl-C}$ composite and (B) cycling performance. (C) Galvanostatic potential profiles of the $\text{Li}_6\text{PS}_5\text{Cl-C}$ composite (5/1 w/w, SSE/carbon). (D) Galvanostatic potential profiles of solvent-mixed cathode ($f_{\text{PTO}} = 50 \text{ wt}\%$) with Super C65 and VGCF (both 10 wt%) as the conductive additive.

Figure S16 shows the quantification of capacity contributed by the redox of $\text{Li}_6\text{PS}_5\text{Cl}$. Due to the low intrinsic electronic conductivity of $\text{Li}_6\text{PS}_5\text{Cl}$, a significant amount of carbon ($\sim 30 \text{ wt}\%$) and vigorous mixing with $\text{Li}_6\text{PS}_5\text{Cl}$ (e.g. ball-milling) are generally required.^{7,18} A high amount of carbon provides more contacting area with the $\text{Li}_6\text{PS}_5\text{Cl}$ leading to a more sufficient redox of $\text{Li}_6\text{PS}_5\text{Cl}$. The amount of carbon in the solvent-mixed and dry-mixed cathodes is kept at 10 wt%, therefore, the highest carbon-to- $\text{Li}_6\text{PS}_5\text{Cl}$ ratio reaches 1:4 at $f_{\text{PTO}} = 50 \text{ wt}\%$. In order to mimic the environment of solvent-mixed cathodes, the $\text{Li}_6\text{PS}_5\text{Cl-C}$ composite was prepared. The cell with 1.75 mg of cathode was assembled, which has exactly the same amount of $\text{Li}_6\text{PS}_5\text{Cl}$ (1.4 mg) and conductive carbon (0.35 mg) as that in a solvent-mixed cathode ($f_{\text{PTO}} = 50 \text{ wt}\%$). The cell was cycled under galvanostatic condition at $55 \mu\text{A cm}^{-2}$ (the current density of the solvent-mixed cathode at $f_{\text{PTO}} = 50 \text{ wt}\%$ for 0.1C). It is observed that even with a high content of conductive carbon (25 wt%), $\text{Li}_6\text{PS}_5\text{Cl}$ exhibits a mere specific capacity of $\sim 15 \text{ mAh g}^{-1}$, corresponding to a total capacity of $\sim 0.02 \text{ mAh}$. Please note that the decomposition of $\text{Li}_6\text{PS}_5\text{Cl}$ in a solvent-mixed cathode will be less because conductive carbon will also sustain the contact with PTO. The solvent-mixed cathode exhibits a high reversible capacity of $>0.5 \text{ mAh}$ at $f_{\text{PTO}} = 50 \text{ wt}\%$, suggesting that the decomposition of $\text{Li}_6\text{PS}_5\text{Cl}$ would contribute at most 4% of the reversible capacity. And this fraction is further decreased with lower carbon-to- $\text{Li}_6\text{PS}_5\text{Cl}$ ratio of the solvent-mixed cathodes ($f_{\text{PTO}} = 30$ and $40 \text{ wt}\%$). A detailed analysis on the cathode capacity contribution from individual component is summarized in supplemental note S3.

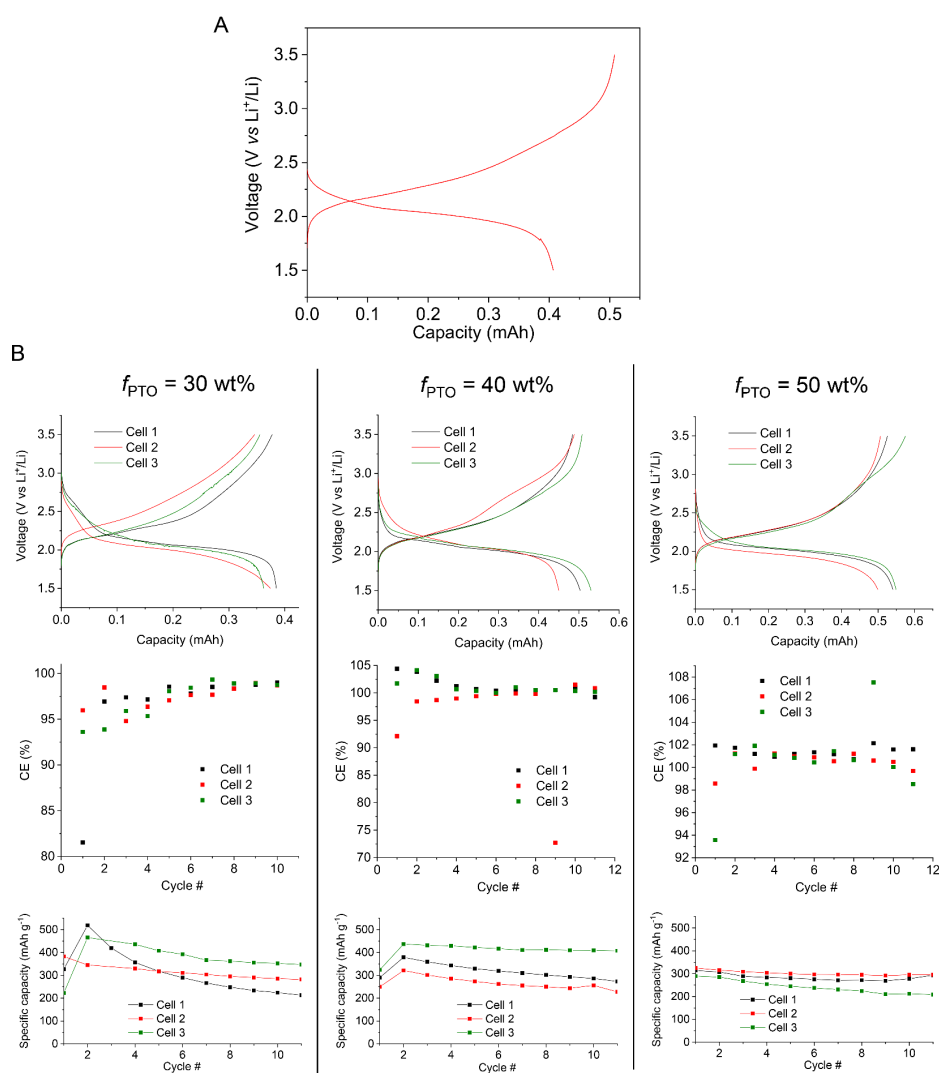


Figure S17. (A) First cycle galvanostatic potential profiles of solvent-mixed cathode ($f_{\text{PTO}} = 40 \text{ wt\%}$). (B) Multiple cell results at different f_{PTO} .

We investigated the first cycle capacity mismatch to quantify the capacity from PTO redox within interphase. A portion of PTO is reduced to Li_xPTO that locates in the interphase and will not contribute to the 1st cycle discharge capacity. As shown in Figure S17, the cathode exhibits 0.41 and 0.51 mAh during the initial discharge and charge, respectively. The 0.1 mAh difference of capacity is due to the lithiation of PTO during the formation of interphase. Therefore, ~80% of the cathode capacity is from the redox of bulk PTO.

Furthermore, we provided the additional cell data at different f_{PTO} regarding the utilization. Since the fabrication of all-solid-state batteries is a multi-step and complicated process, a deviation in device performance is expected. As shown above, we provide data for in total 9 cells (3 replicates for each f_{PTO}). For each f_{PTO} , we showed the results with lowest, moderate, and best utilization of PTO. There are some cell-to-cell variations, as fabrication from various batches are conducted, but in general the performance agrees quite well. The capacity values of solvent-mixed cathodes are: $f_{\text{PTO}} (30\%)$: $0.3738 \pm 0.0110 \text{ mAh}$. $f_{\text{PTO}} (40\%)$: $0.5171 \pm 0.0615 \text{ mAh}$. $f_{\text{PTO}} (50\%)$: $0.5297 \pm 0.0267 \text{ mAh}$. And the corresponding CEs are: $f_{\text{PTO}} (30\%)$: $98.8 \pm 0.2\%$. $f_{\text{PTO}} (40\%)$: $100.0 \pm 0.8\%$. $f_{\text{PTO}} (50\%)$: $99.9 \pm 1.4\%$.

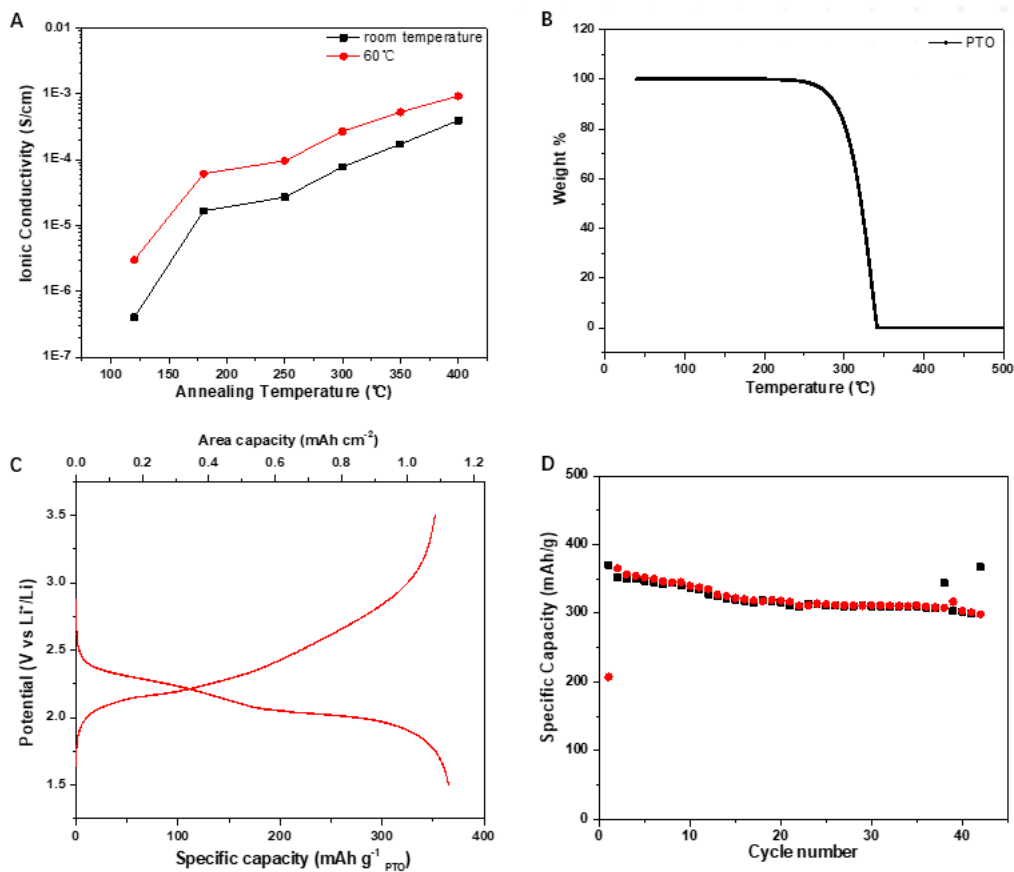
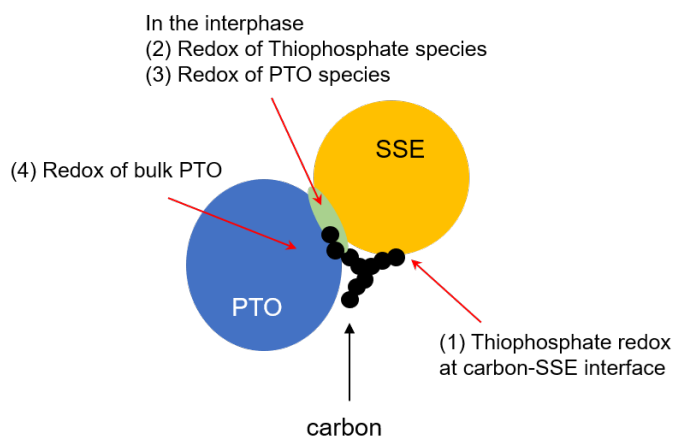


Figure S18. (A) Relationship between ionic conductivity and annealing temperature for pristine Li₆PS₅Cl after solution process with ethanol. (B) Thermogravimetric analysis plot of PTO. (C) Voltage profile of a PTO cell with 10 mg cathode loading, reaching areal capacity of 1.1 mAh cm⁻². (D) cycle stability.

Since PTO starts sublimation at 250 °C, to prevent PTO sublimation, we choose to anneal the solvent-mixed cathode at 180 °C in this work. At this temperature, the crystallinity of Li₆PS₅Cl has not been fully recovered. The measurement shows the ionic conductivity of pure phase Li₆PS₅Cl after annealing is 6.2×10^{-5} S/cm (60 °C). Various annealing conditions will be explored in the future to optimize the composite electrode performance.

Supplemental scheme



Scheme S1. Schematic illustration on the redox process in a composite cathode. (1) redox of thiophosphate at the SSE/carbon interface, redox of (2) thiophosphate species and (3) Li_xPTO species in the interphase, and (4) redox of bulk PTO. The size of different phase may not be proportional.

Supplemental tables

Table S1. Comparison of the electrode-level specific energy with literatures which uses lithium thiophosphates electrolytes. DP: dry-mixed; SP: solvent-mixed.

#	CAM ^a	f_{CAM} (wt%) ^b	Electrolyte ^c	Anode	Temp. (°C)	C_s (mAh g^{-1}) ^d	V (V vs Li ^{+/} Li) ^e	\bar{E}_{CAM} (Wh kg^{-1}) ^f	$\bar{E}_{Electrode}$ (Wh kg^{-1}) ^g	Reference
1	NMC622	70	Li ₇ P ₂ S ₈ l	Li	55	168	~3.70	621	435	19
2	NMC622	70	Li _{6.6} P _{0.4} Ge _{0.6} S ₅ l	Li ₄ Ti ₅ O ₁₂	60	89	~3.65	325	228	20
3	NMC622	67	Li ₃ PS ₄ , PEO-LiTFSI	Li	60	139	~3.73	518	348	21
4	NMC811	86	Li ₆ PS ₅ Cl	Li	60	215	~3.76	808	695	22
5	LiCoO ₂	70	75Li ₂ S:25P ₂ S ₅ Glass	Graphite	60	110	~3.80	418	293	23
6	LiCoO ₂	70	70 Li ₂ S :30 P ₂ S ₅ GC	Graphite	60	90	~3.80	342	239	23
7	NCA	46	Li ₃ PS ₄ -S-PES	Li-In	60	156	~3.75	585	268	24
8	PBALS	25	Li ₃ PS ₄	Li	NA	128	~1.40	179	45	25
9	DP-PTO (cryo-milling)	20	Li ₃ PS ₄	Li	60	407	~2.10	828	165	26
10	DP-PTO	20	Li ₃ PS ₄	Li	60	323	~2.10	678	122	This work
11	DP-PTO	30	Li ₃ PS ₄	Li	60	271	~2.10	526	158	This work
12	DP-PTO	40	Li ₃ PS ₄	Li	60	220	~2.10	417	166	This work
13	DP-PTO	50	Li ₃ PS ₄	Li	60	134	~2.10	243	122	This work
14	SP-PTO	30	Li ₃ PS ₄	Li	60	345	~2.10	659	197	This work
15	SP-PTO	40	Li ₃ PS ₄	Li	60	359	~2.10	658	263	This work
16	SP-PTO-BM	40	Li ₃ PS ₄	Li	60	399	~2.10	755	302	This work
17	SP-PTO	50	Li ₃ PS ₄	Li	60	308	~2.10	558	279	This work

^a NMC622 (LiNi_{0.6}Mn_{0.2}Co_{0.2}O₂); NCA (LiNi_{0.80}Co_{0.15}Al_{0.05}O₂); PBALS (4-(phenylazo) benzoic acid lithium salt).

^b f_{CAM} is calculated based on the reported mass ratio of the composite cathodes.

^c LiTFSI (Lithium bis(trifluoromethanesulfonyl)imide); PES (polyethylene sulfide); GC: glass-ceramic. "Electrolyte" describes the separator.

^d Data extracted from descriptions and figures of each reference.

^e Average discharge potential values extracted from figures of each reference.

^f Calculated based on the mass of CAM in the composite cathodes. For CAMs that do not contain Li, stoichiometric Li is included in the E_{CAM} calculation, e.g. $4\text{Li} + \text{PTO} \leftrightarrow \text{Li}_4\text{PTO}$.

^g Calculated based on total mass of the composite cathodes.

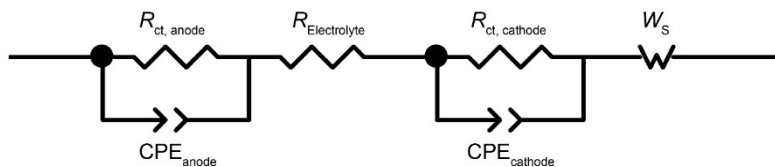
Table S2. ToF-SIMS data summary.

m/z	Possible fragment composition	Origin	Figure entry
304.8	Cs_2LiS^+		Figure 8a, Figure 9a
178.9	CsLi_2S^+	$\text{Li}_6\text{PS}_5\text{Cl}$ phase	Figure 8b, Figure 9b
6.0	${}^6\text{Li}^+$		Figure 8c, Figure 9c
25.0	C_2H^-		Figure 9d
290.8	$\text{Cs}_2\text{C}_2\text{H}^+$	PTO phase	Figure 8d
422.7	Cs_3C_2^+		Figure 8e, Figure 9e
446.7	Cs_3C_4^+		Figure 8f, Figure 9f
296.8	$\text{Cs}_2\text{LiC}_2^+$	PTO- $\text{Li}_6\text{PS}_5\text{Cl}$	Figure 8g, Figure 9g
320.8	$\text{Cs}_2\text{LiC}_4^+$	interphase	Figure 8h, Figure 9h
		Overlay	Figure 8i
			Figure 9i
32.0	S^-	$\text{Li}_6\text{PS}_5\text{Cl}$ phase	Figure 9j
63.9	S_2^-	$\text{Li}_6\text{PS}_5\text{Cl}$ phase	Figure 9j
134.9	LiS_4^-	$\text{Li}_6\text{PS}_5\text{Cl}$ phase	Figure 9j
77.0	LiCl_2^-	$\text{Li}_6\text{PS}_5\text{Cl}$ phase	Figure 9j

Table S3. The Warburg coefficient of SP cathode ($f_{\text{PTO}} = 40 \text{ wt}\%$).

Process time (h)	0	3.4	7.1	8.0	11.5	15.1	20.8	24.3	27.9
Potential (V vs Li ⁺ /Li)	2.43	2.05	1.88	1.50	2.26	2.55	3.50	2.15	2.06
A_W ($\Omega \text{ s}^{-1/2}$)	62	31	34	47	42	64	1310	114	55
Process time (h)	32.6	36.1	39.5	43.4	46.9	50.5	54.4	58.0	61.3
Potential (V vs Li ⁺ /Li)	1.50	2.27	2.58	3.50	2.10	2.04	1.50	2.27	2.53
A_W ($\Omega \text{ s}^{-1/2}$)	59	59	136	1404	107	56	66	71	171
Process time (h)	65.1	68.7	72.3	75.8					
Potential (V vs Li ⁺ /Li)	3.50	2.08	2.03	1.50					
A_W ($\Omega \text{ s}^{-1/2}$)	1435	106	61	73					

Table S4. Equivalent circuit and fitting parameters for the EIS Spectra of dry-mixed and solvent-mixed PTO cathodes ($f_{\text{PTO}} = 40 \text{ wt}\%$). $R_{\text{Electrolyte}}$: resistance of electrolyte layer, including bulk and grain boundary resistance; R_{ct} and CPE: charge transfer resistance and constant phase element of Li-SE interface, and PTO- $\text{Li}_6\text{PS}_5\text{Cl}$ interphase. W_s : Warburg element.



Dry-mixed			Solvent-mixed		
Potential	Capacity	$R_{\text{ct, Cathode}}$	Potential	Capacity	$R_{\text{ct, Cathode}}$
(V vs Li^+/Li)	($\text{mAh g}^{-1}_{\text{PTO}}$)	(Ω)	(V vs Li^+/Li)	($\text{mAh g}^{-1}_{\text{PTO}}$)	(Ω)
2.80	0	24	2.43	0	15
2.17	163	32	2.05	123	15
2.02	327	28	1.88	245	13
1.50	420	19	1.50	268	31
2.22	82	35	2.26	123	15
2.46	165	40	2.55	245	20
3.50	230	153	3.50	430	185

$R_{\text{ct, Cathode}}$ of both dry-mixed and solvent-mixed cathodes show relatively small values and remained stable within the operating voltage window. The sharp increase at the end of charge (3.5 V vs Li^+/Li) indicates the accumulation of Li-PS_n at the PTO- $\text{Li}_6\text{PS}_5\text{Cl}$ interphase which hinders the charge-transfer kinetics.

Table S5. Summary of calculated volume fraction of cathode components and volumetric energy density of PTO electrodes based on following density values: PTO (1.5 g cm^{-3}), $\text{Li}_6\text{PS}_5\text{Cl}$ (1.64 g cm^{-3}) and super C65 (1.6 g cm^{-3}). DP: dry-mixed; SP: solvent-mixed.

#	CAM	f_{CAM} (wt%)	f_{CAM} (v%)	f_{SE} (v%)	f_{Carbon} (v%)	Cathode Density (g cm^{-3})	E_{Cathode} (Wh L^{-1})
1	DP-PTO	20	21.4	68.6	10.0	1.60	226
2	DP-PTO	30	31.9	58.2	9.9	1.59	278
3	DP-PTO	40	42.1	48.1	9.8	1.58	265
4	DP-PTO	50	52.1	38.1	9.8	1.56	210
5	SP-PTO	30	31.9	58.2	9.9	1.59	348
6	SP-PTO	40	42.1	48.1	9.8	1.58	460
7	SP-BM-PTO	40	42.1	48.1	9.8	1.58	527
8	SP-PTO	50	52.1	38.1	9.8	1.56	483

Supplemental Notes

Note S1. Detailed analysis on the UV-Vis identification of Li_xPTO and possible effects from lithium polysulfides.

In order to confirm our identification on the formation of Li_xPTO and avoid possible effects from lithium polysulfides, we use chemically synthesized Li_xPTO as the reference. A comprehensive investigation on the chemical/electrochemical properties of Li_xPTO is beyond the current scope and will be reported in future study.

First of all, the intrinsic oxidizing strength of PTO suggests that lithium polysulfides will not form by the spontaneous redox between PTO and $\text{Li}_6\text{PS}_5\text{Cl}$. The redox potentials of quinones originate from the energy level of lowest unoccupied molecular orbitals (LUMOs) and can be experimentally identified. As shown in the experimental data (Figure S4), PTO has an OCP beyond the stability window of $\text{Li}_6\text{PS}_5\text{Cl}$, as we have discussed, and will oxidize $\text{Li}_6\text{PS}_5\text{Cl}$ to form lithiated PTO (Li_xPTO , carbonyl moieties are reduced to enolate-like structure). Oxidation of $\text{Li}_6\text{PS}_5\text{Cl}$ has been recently studied.⁷ It is found that the oxidation occurs at the P-S-Li moieties coupled with delithiation. The oxidation starts from the rise of chemical valence of S^{2-} to S^- to form bridging sulfur ($-\text{[S]}_n^-$) with Li^+ extracted, resulting in polythiophosphates.² Under a higher oxidizing potential (>4 V vs Li^+/Li), the P-S-Li moieties will be fully oxidized to P_2S_5 and elemental sulfur. Since the oxidation of $\text{Li}_6\text{PS}_5\text{Cl}$ is a process losing Li^+ , there is no mechanism supporting the formation of lithium polysulfides under the oxidative environment by PTO. Additionally, the electrochemistry study of lithium-sulfur batteries²⁷ provides a reference at molecular level that lithium polysulfides will be oxidized (delithiated) at potentials beyond ~ 2.8 V vs Li^+/Li .

Second, the multi-step redox process of PTO enables us to chemically synthesize Li_xPTO for UV-Vis analysis. Although the UV-Vis spectroscopy of Li-S systems has been investigated, study on organic cathode materials has not yet been done. And more specifically, no spectroscopic study has been conducted on the reduction intermediates (such as Li_xPTO) of PTO, hence, no direct reference on the UV-Vis of Li_xPTO is available from the public domain. We chemically synthesized the partially lithiated PTO (Li_xPTO , x is ~ 2) and fully lithiated PTO (Li_4PTO), note that a detailed synthesis procedure and analysis on properties of these PTO derivatives will be reported elsewhere. The FTIR spectra (Figure S4) shows the evolution of carbonyls under different lithiation states. Furthermore, a direct comparison between the UV-Vis spectra of chemically synthesized Li_xPTO and that of Figure 3B is provided in Figure S4, the characteristic peaks at 380, 500 and 580 nm match well with the solvent-mixed sample across the spectra. Li_4PTO is insoluble and will not contribute to absorption. This new data serves as a solid experimental evidence showing the formation of Li_xPTO .

Third, we compare the spectra of Li_xPTO with those of polysulfides. Although the formation of polysulfide is not thermodynamically favored, the interference from polysulfide can be ruled out by comparing the spectra of Li_xPTO and lithium polysulfides (spectrum can be found in literature²⁸). Polysulfides have characteristic absorptions in the region of 300-450 nm with the lowest vibronic transition peak at ~ 420 nm. However, the characteristic peaks of Li_xPTO appears at 380, 500 and 580 nm. For example, the peak at 420 nm of lithium polysulfides is absent. The difference in characteristic peaks further confirms the assignments of Li_xPTO .

Note S2. Detailed analysis on the multiple interfaces that may undergo electrochemical process within cathode.

Since PTO and $\text{Li}_6\text{PS}_5\text{Cl}$ are both poorly electronic conductive, the electrochemical reactions take place at their contact with carbon additive. Four processes (Scheme S1) may take place within a composited cathode: (1) redox of thiophosphate at the SSE/carbon interface, (2) redox of thiophosphate species, (3) redox of Li_xPTO species in the interphase, and (4) redox of bulk PTO. In this section, we will provide additional analysis on the spectroscopic part. And a detailed discussion on the capacity contributed by each process is shown in supplemental note S3.

The first thing we need to address is what species is redox active within the voltage window (1.5-3.5 V vs Li^+/Li). The electrochemistry of $\text{Li}_6\text{PS}_5\text{Cl}$ is complicated. A recent study⁷ found that the reductive decomposition of PS_4 unit towards formation of Li_3P and Li_2S occurs at ~ 1.1 V (vs Li^+/Li). Additionally, oxidation of Cl^- may happen under extremely high voltage couple due to the high electronegativity. Therefore, the major redox active species is PS_4 units (P-S-Li moieties). Oxidation of $\text{Li}_6\text{PS}_5\text{Cl}$ may result in different products depending on the applied voltage. For example, when the voltage slightly exceeds the stability window of $\text{Li}_6\text{PS}_5\text{Cl}$, S(-2) starts to be oxidized and Li^+ is extracted. Under this condition, the neighboring PS_4 units are linked by S-S bond ($-\text{[S]}_n^-$) which is the poly-thiophosphates, and ionic conductivity starts to decrease. As more and more S(-2) is oxidized and Li^+ is extracted, the content of $-\text{[S]}_n^-$ increased and the ionic conductivity is further decreased. The fully oxidized products (~ 4.2 V vs Li^+/Li) would be P_2S_5 and S under DFT-based theoretical predication, and they may be observed under certain conditions.⁷ Formation of P_2S_5 and S will severely passivate the surface of carbon and render the redox much less reversible.²⁹

The electrochemical reversibility the interphase has been discussed in the main text, whereas, how to distinguish the XPS signal contribute by thiophosphate redox at CAM/SSE and carbon/SSE interface remains a challenge. Walther et al. provided the schematic model showing the redox of thiophosphate at several interface, however, a numerical assignment remains to be unrevealed.³⁰ Besides, there is no report on XPS spectroscopic method that can provide such a high spatial resolution to directly focus on the interface. Hence a direct XPS characterization on multiple interfaces is impractical.

Alternatively, we would like to provide several evidences to show that the S 2p signal mainly originates from the the interphase in our study. First of all, the amount of carbon is optimized to reach a high utilization of PTO with minimum decomposition of electrolyte.^{4,26} Therefore, the carbon/SSE interface is expected to be minimized. Additionally, during the solvent-mixing, we mixed PTO with Super C65 to ensure a good homogenization, which also helps to prevent the formation “isolated carbon” (carbon that is not in contact with PTO), that leads to carbon/SSE contact.

In addition to the practical methods to reduce carbon/SSE interface, we proposed an analysis that could qualitatively demonstrate that the S 2p signal mainly originates from the CAM/SSE interface (the redox of thiophosphate species within interphase). During the electrode preparation, $\text{Li}_6\text{PS}_5\text{Cl}$ is oxidized to poly-thiophosphate species that contributes to the S 2p_{3/2} component at 163.6 eV. This redox particularly occurs at PTO- $\text{Li}_6\text{PS}_5\text{Cl}$ contact, whereas a contact between carbon and $\text{Li}_6\text{PS}_5\text{Cl}$ may not lead to the redox. Therefore, the 163.6 eV component in the pristine cathode originates from the interphase. After the cathode is discharge and charged (Figure 5C), those $\text{Li}_6\text{PS}_5\text{Cl}$ at the carbon/SSE interface will also be oxidized to poly-thiophosphate species. Hence the 163.6 eV component from a

charged cathode comes from poly-thiophosphate species in both the interphase (process (2) in Scheme S1) and the carbon/SSE interface (process (1) in Scheme S1). Therefore, if the S 2p signal is mainly from carbon/SSE interface, we should expect a significant increase of 163.6 eV component in the charged cathode. However, mere change is observed from both dry- and solvent-mixed cathodes, suggesting that the S 2p signal is mainly from the interphase.

The CAM/SSE interface of PTO-thiophosphate system is also evaluated according to a previously reported method.^{4,26} The good correlation between capacity, voltage and Warburg coefficient also suggests that the CAM/SSE interface accounts for the observed electrochemical reversibility.

Note S3. Detailed analysis on the cathode capacity contributed by cathode components.

Multiple redox processes happen in the composite cathode (Scheme S1). Indeed, this is a picture that fits not only our PTO-Li₆PS₅Cl system but also any composite cathodes with redox-active electrolytes. Typically, these processes may include (1) redox of thiophosphate at the SSE/carbon interface, redox of (2) thiophosphate species and (3) PTO species in the interphase, and (4) redox of bulk PTO. (1) and (2) contribute to extra capacity in addition to the capacity from PTO of (3) and (4).

To quantify the capacity from (1) and (2), we need to figure out how these processes could occur. Due to the low electronic conductivity of Li₆PS₅Cl and PTO, the electronic conduction is essential to sustain their redox. Ideally, carbon should be utilized at the CAM/SSE interface and extra carbon may lead to the situation of (1). A proper amount of carbon additive is required. We have previously shown that 10 wt% of Super C65 is an optimized condition to maximize PTO utilization and minimize the electrolyte decomposition.^{4,26} Hence 10 wt% of Super C65 is adopted in this study.

The redox of thiophosphates generally happens at the interface with conductive carbon.^{7,14} Based on this property, we designed the control sample (Li₆PS₅Cl-C electrode) with conditions as close to a PTO cathode as possible. Two control samples are prepared: one has 1.75 mg Li₆PS₅Cl and 0.35 mg Super C65 (5/1 w/w SSE/carbon) that corresponds to the mass loading of a cathode at $f_{\text{PTO}} = 40$ wt% (1.40 mg PTO, 1.75 mg Li₆PS₅Cl and 0.35 mg Super C65). And the other one has 1.40 mg Li₆PS₅Cl and 0.35 mg Super C65 (4/1 w/w SSE/carbon) that corresponds to the mass loading of a cathode at $f_{\text{PTO}} = 50$ wt% (1.75 mg PTO, 1.40 mg Li₆PS₅Cl and 0.35 mg Super C65). Li₆PS₅Cl was treated by ethanol and the voltage window is set the same as a PTO cathode (1.5-3.5 V vs Li⁺/Li).

The electrochemical performance of control sample is summarized in Figure S16. As shown in Figure S16A and C, a higher carbon content (C-Li₆PS₅Cl ratio), rather than the amount of Li₆PS₅Cl, leads to a higher redox capacity. This is reasonable since a higher carbon content results in more carbon/SSE interface. Among the solvent-mixed cathodes, the highest C-Li₆PS₅Cl ratio is reached when $f_{\text{PTO}} = 50$ wt%. The control sample (1.40 mg Li₆PS₅Cl and 0.35 mg) presents an extreme condition where all the carbon is utilized to sustain the redox of SSE, and no electronic conduction is used for PTO. Under such condition the capacity from SSE redox is maximized as ~0.02 mAh. The capacity remains stable upon cycling that rules out the possibility of accumulative contribution (Figure S16B). Furthermore, it is a reasonable hypothesis that when PTO is presented in the cathode, the carbon/SSE interface will be less and the capacity from SSE redox is decreased. Note that the cathode capacity is above 0.5 mAh at $f_{\text{PTO}} = 50$ wt%, the SSE redox contributes to <4% of total capacity. The polythiophosphate induced by interfacial redox with PTO cannot be achieved in the control sample. But these species are expected to have similar electrochemical behavior during cycling, because the oxidizing strength of PTO is within 1.5-3.5 V vs Li⁺/Li. Therefore, the control sample provides an estimation on the total capacity from SSE redox including process (1) and (2). Although a rigid distinguishment between process (1) and (2) is not applicable, the data could be a suitable reference in our study suggesting that the overall contribution is <4%.

Another evidence showing that capacity mostly originates from PTO is the electrode-level capacity of solvent-mixed cathodes with different f_{PTO} (Figure 6A). If the redox of Li₆PS₅Cl contributes to the major capacity, a higher electrode-level capacity is expected at $f_{\text{PTO}} = 30$ wt%, where the highest amount of Li₆PS₅Cl is achieved (2.1 mg) given the same carbon loading (0.35 mg). However, the experimental data shows that higher amount of PTO, not Li₆PS₅Cl, leads to a significantly higher electrode-level capacity. Furthermore, we also evaluated the effects of different carbon additive (Figure S16D). Solvent-

mixed cathode ($f_{\text{PTO}} = 50 \text{ wt\%}$) with Super C65 and VGCF (both 10 wt%) The cathode with VGCF exhibits $\sim 0.035 \text{ mAh}$ lower capacity than that with Super C65, very likely due to the less surface area that can sustain the electronic conductivity for PTO. The difference in capacity, 0.035 mAh , exceeds the maximum available capacity from thiophosphate redox with Super C65 (0.02 mAh). This observation also suggests that the electrode capacity contributed by thiophosphate redox is minor.

As for the capacity from PTO redox of (3) and (4), we can provide a brief estimate on the capacity of PTO species in the interphase (3), as we discussed above in comment 3. Because the capacity from SSE species is much lower than that from PTO redox, it is reasonable to assume most cell capacity is from PTO redox. Due to the spontaneous redox between PTO and $\text{Li}_6\text{PS}_5\text{Cl}$, a portion of PTO is reduced to Li_xPTO that locates in the interphase. And these species will not contribute to the 1st cycle discharge capacity. Therefore, the discharge capacity is less than charge capacity in 1st cycle. Figure S17 reveals 0.1 mAh difference in discharge (0.41 mAh) and charge (0.51 mAh) capacity, due to the lithiation of PTO during the formation of interphase. Assuming $\text{Li}_6\text{PS}_5\text{Cl}$ reaches a maximum at 4% (0.02 mAh) of total capacity (0.51 mAh), the redox of bulk PTO contributes to 0.392 mAh ($\sim 77\%$ of total capacity), and PTO in interphase contributes to 0.098 mAh ($\sim 19\%$ of total capacity). The redox of PTO in solid-state electrodes has been previously studied by our group,^{4,26,31} and we found that the utilization of PTO is high as long as good electronic/ionic conduction is maintained. It should be noted that quantitative assignment of each electrode component contribution remains challenging, and, from practical perspective, it makes more sense to evaluate the electrode-level specific capacity and specific energy by considering the total electrode mass, as demonstrated in this work.

References

1. Zhu, Y., He, X. & Mo, Y. (2015). Origin of outstanding stability in the lithium solid electrolyte materials: insights from thermodynamic analyses based on first-principles calculations. *ACS Appl. Mater. Interfaces* 7, 23685-23693.
2. Koerver, R. *et al.* (2017). Redox-active cathode interphases in solid-state batteries. *J. Mater. Chem. A* 5, 22750-22760.
3. Nokami, T. *et al.* (2012). Polymer-Bound Pyrene-4,5,9,10-tetraone for Fast-Charge and -Discharge Lithium-Ion Batteries with High Capacity. *J. Am. Chem. Soc.* 134, 19694-19700.
4. Hao, F. *et al.* (2019). Taming active material-solid electrolyte interfaces with organic cathode for all-solid-state batteries. *Joule* 3, 1349-1359.
5. Troltzsch, U., Kanoun, O. & Trankler, H. R. (2006). Characterizing aging effects of lithium ion batteries by impedance spectroscopy. *Electrochim. Acta* 51, 1664-1672.
6. Koerver, R. *et al.* (2017). Capacity fade in solid-state batteries: interphase formation and chemomechanical processes in nickel-rich layered oxide cathodes and lithium thiophosphate solid electrolytes. *Chem. Mater.* 29, 5574-5582.
7. Tan, D. H. S. *et al.* (2019). Elucidating reversible electrochemical redox of Li6PS5Cl solid electrolyte. *ACS Energy Lett.* 4, 2418-2427.
8. Auvergniot, J. *et al.* (2017). Redox activity of argyrodite Li6PS5Cl electrolyte in all-solid-state Li-ion battery: An XPS study. *Solid State Ion.* 300, 78-85.
9. Mayeux, C. *et al.* (2009). Interaction of the cesium cation with mono-, di-, and tricarboxylic acids in the gas phase. A Cs⁺ affinity scale for cesium carboxylates ion pairs. *J. Am. Soc. Mass Spectrom* 20, 1912-1924.
10. Gupta, A. K. & Krishnamurthy, M. (2003). Fragmentation of cesium-carbon cluster anions. *Phys. Rev. A* 67, 023201.
11. Braim, S. A., Shakesheff, K. M., Saunders, B. R. & Alexander, C. (2016). Thermoresponsive magnetic colloidal gels via surface-initiated polymerisation from functional microparticles. *J. Mater. Chem. B* 4, 962-972.
12. Hinder, S. J., Lowe, C. & Watts, J. F. (2007). ToF-SIMS depth profiling of a complex polymeric coating employing a C60 sputter source. *Surf. Interface Anal.* 39, 467-475.
13. Walther, F. *et al.* (2019). Visualization of the Interfacial Decomposition of Composite Cathodes in Argyrodite-Based All-Solid-State Batteries Using Time-of-Flight Secondary-Ion Mass Spectrometry. *Chem. Mater.* 31, 3745-3755.
14. Swamy, T., Chen, X. & Chiang, Y.-M. (2019). Electrochemical redox behavior of Li ion conducting sulfide solid electrolytes. *Chem. Mater.* 31, 707-713.
15. Xiao, Y. *et al.* (2020). Understanding interface stability in solid-state batteries. *Nat. Rev. Mater.* 5, 105-126.
16. Zhao, Y., Zheng, K. & Sun, X. (2018). Addressing interfacial issues in liquid-based and solid-state batteries by atomic and molecular layer deposition. *Joule* 2, 2583-2604.
17. Sun, C., Liu, J., Gong, Y., Wilkinson, D. P. & Zhang, J. (2017). Recent advances in all-solid-state rechargeable lithium batteries. *Nano Energy* 33, 363-386.
18. Schwietert, T. K. *et al.* (2020). Clarifying the relationship between redox activity and electrochemical stability in solid electrolytes. *Nat. Mater.* 19, 428-435.
19. Choi, S. J. *et al.* (2018). LiI-Doped Sulfide Solid Electrolyte: Enabling a High-Capacity Slurry-Cast Electrode by Low-Temperature Post-Sintering for Practical All-Solid-State Lithium Batteries. *ACS*

- Appl. Mater. Interfaces 10, 31404-31412.
20. Kraft, M. A. *et al.* (2018). Inducing High Ionic Conductivity in the Lithium Superionic Argyrodites $\text{Li}_{6+x}\text{P}_{(1-x)}\text{Ge}_x\text{S}_{(5)}$ for All-Solid-State Batteries. *J. Am. Chem. Soc.* 140, 16330-16339.
 21. Ates, T., Keller, M., Kulisch, J., Adermann, T. & Passerini, S. (2019). Development of an all-solid-state lithium battery by slurry-coating procedures using a sulfidic electrolyte. *Energy Storage Mater.* 17, 204-210.
 22. Lee, Y. G. *et al.* (2020). High-energy long-cycling all-solid-state lithium metal batteries enabled by silver-carbon composite anodes. *Nat. Energy* 5, 299-308.
 23. Ohtomo, T. *et al.* (2013). All-solid-state lithium secondary batteries using the $75\text{Li}_{(2)}\text{S}$ center dot $25\text{P}_{(2)}\text{S}_{(5)}$ glass and the $70\text{Li}_{(2)}\text{S}$ center dot $30\text{P}_{(2)}\text{S}_{(5)}$ glass-ceramic as solid electrolytes. *J. Power Sources* 233, 231-235.
 24. Li, Y. J. *et al.* (2020). Thin Solid Electrolyte Layers Enabled by Nanoscopic Polymer Binding. *ACS Energy Lett.* 5, 955-961.
 25. Luo, C. *et al.* (2018). Solid-State Electrolyte Anchored with a Carboxylated Azo Compound for All-Solid-State Lithium Batteries. *Angew Chem Int Edit* 57, 8567-8571.
 26. Hao, F. *et al.* (2021). High-Energy All-Solid-State Organic-Lithium Batteries Based on Ceramic Electrolytes. *ACS Energy Lett.* 6, 201-207.
 27. Manthiram, A., Fu, Y. Z., Chung, S. H., Zu, C. X. & Su, Y. S. (2014). Rechargeable Lithium-Sulfur Batteries. *Chem. Rev.* 114, 11751-11787.
 28. He, Q., Freiberg, A. T. S., Patel, M. U. M., Qian, S. & Gasteiger, H. A. (2020). Operando Identification of Liquid Intermediates in Lithium-Sulfur Batteries via Transmission UV-vis Spectroscopy. *J. Electrochem. Soc.* 167.
 29. Swamy, T., Chen, X. W. & Chiang, Y. M. (2019). Electrochemical Redox Behavior of Li Ion Conducting Sulfide Solid Electrolytes. *Chem. Mater.* 31, 707-713.
 30. Walther, F. *et al.* (2020). Influence of Carbon Additives on the Decomposition Pathways in Cathodes of Lithium Thiophosphate-Based All-Solid-State Batteries. *Chem. Mater.* 32, 6123-6136.
 31. Chi, X. W. *et al.* (2019). A high-energy quinone-based all-solid-state sodium metal battery. *Nano Energy* 62, 718-724.